Supplementary information for

Measurement report: Sources and meteorology influencing highly-time resolved PM2.5 trace elements at 3 urban sites in extremely polluted Indo Gangetic Plain in India.

Ashutosh K. Shukla[1], Sachchida N. Tripathi[1,2]*, Shamitaksha Talukdar[1], Vishnu Murari[1], Sreenivas Gaddamidi[1], Manousos-Ioannis Manousakas[3], Vipul Lalchandani[1], Kuldeep Dixit[4], Vinayak M. Ruge[5], Peeyush Khare[3], Mayank Kumar[6], Vikram Singh[7], Neeraj Rastogi[8], Suresh Tiwari[9], Atul K. Srivastava[9], Dilip Ganguly[10], Kaspar Rudolf Daellenbach[3], Andre. S. H. Prevot[3]*

[1]Department of Civil Engineering, Indian Institute of Technology Kanpur, Uttar Pradesh, 208016, India
[2]Department of Sustainable Energy Engineering, Indian Institute of Technology Kanpur, Uttar Pradesh, 208016, India
[3]Laboratory of Atmospheric Chemistry, Paul Scherrer Institute, Villigen PSI, 5232, Switzerland
[4]School of Public & International Affairs, Virginia Tech Blacksburg, Virginia, 24060, USA
[5]Tesscorn AeroFluid, Inc. 50, 3rd Floor, 100 Feet Road, Koramangala 2nd Block, Bangalore 560034, India
[6]Department of Mechanical Engineering, Indian Institute of Technology Delhi, New Delhi 110016, India
[7]Department of Chemical Engineering, Indian Institute of Technology Delhi, New Delhi -110016, India
[8]Geosciences Division, Physical Research Laboratory, Ahmedabad, 380009, India
[9]Indian Institute of Tropical Meteorology, Ministry of Earth Sciences, New Delhi, India
[10]Centre for Atmospheric Sciences, Indian Institute of Technology Delhi, New Delhi, 110016, India

 *Correspondence to S. N. Tripathi (snt@iitk.ac.in) and André S. H. Prévôt (andre.prevot@psi.ch)

Contents:

Supplementary text (S1-S7)

Supplementary Figures (S1-S16)
Supplementary Tables (S1- S6)
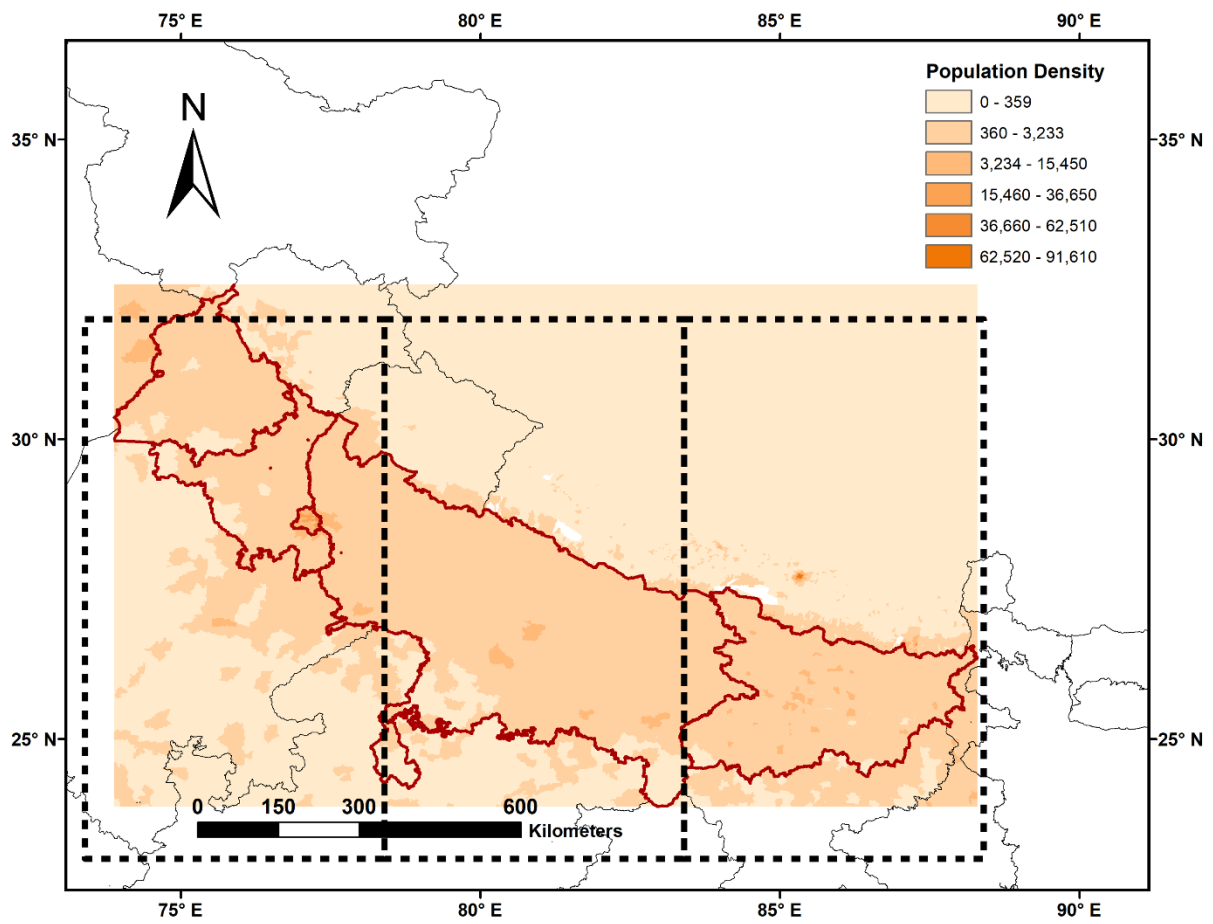
Figure S1. Population density across the IGP region.

(a) Correlation heatmap at U-IGP1

(b) Correlation heatmap at U-IGP2
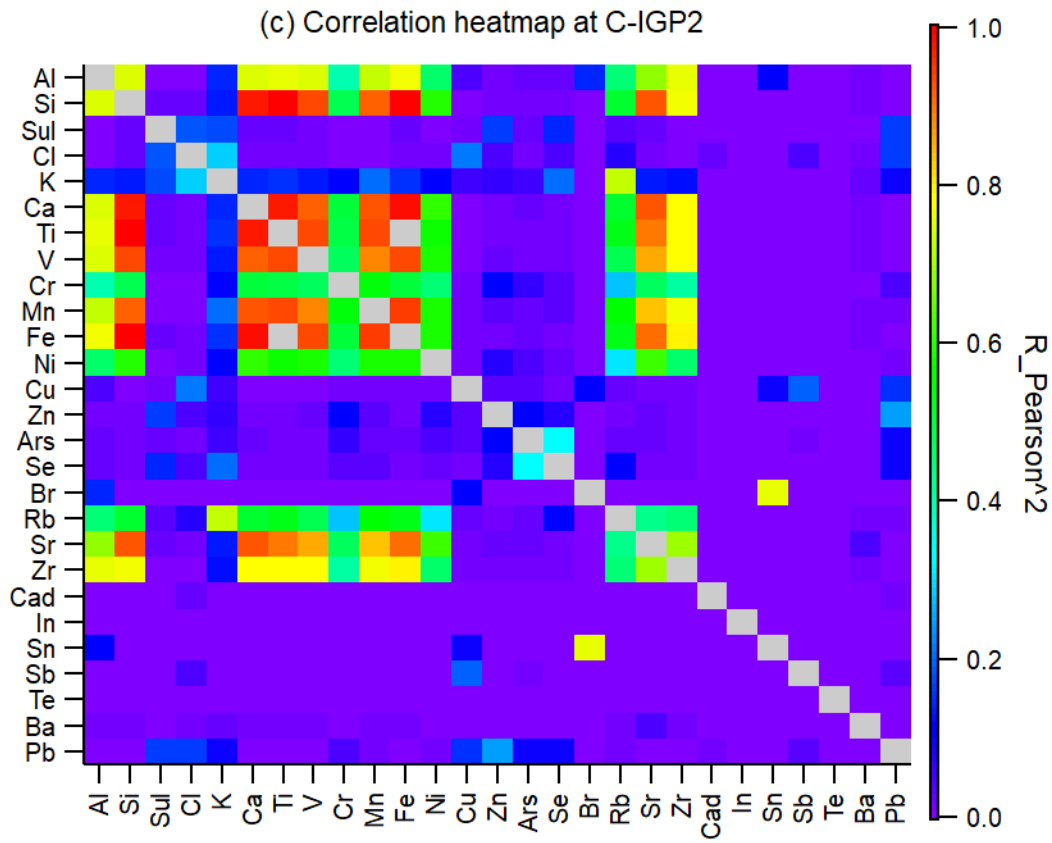
Figure S2. Heatmap showing correlation between the elements measured using Xact at the a)U-IGP1, b) U-IGP2 and c) C-IGP1 site

(a) U-IGP1

(b) U-IGP2

Figure S3. Time series of elemental concentration measured by Xact, RC of elements, variation of PM2.5, fraction of elemental PM to total PM2.5, RH, temperature, wind speed, wind direction, precipitation, solar radiation and PBLH during the measurement period at (a) U-IGP1 and (b) U-IGP2 and (c) C-IGP1 sites.
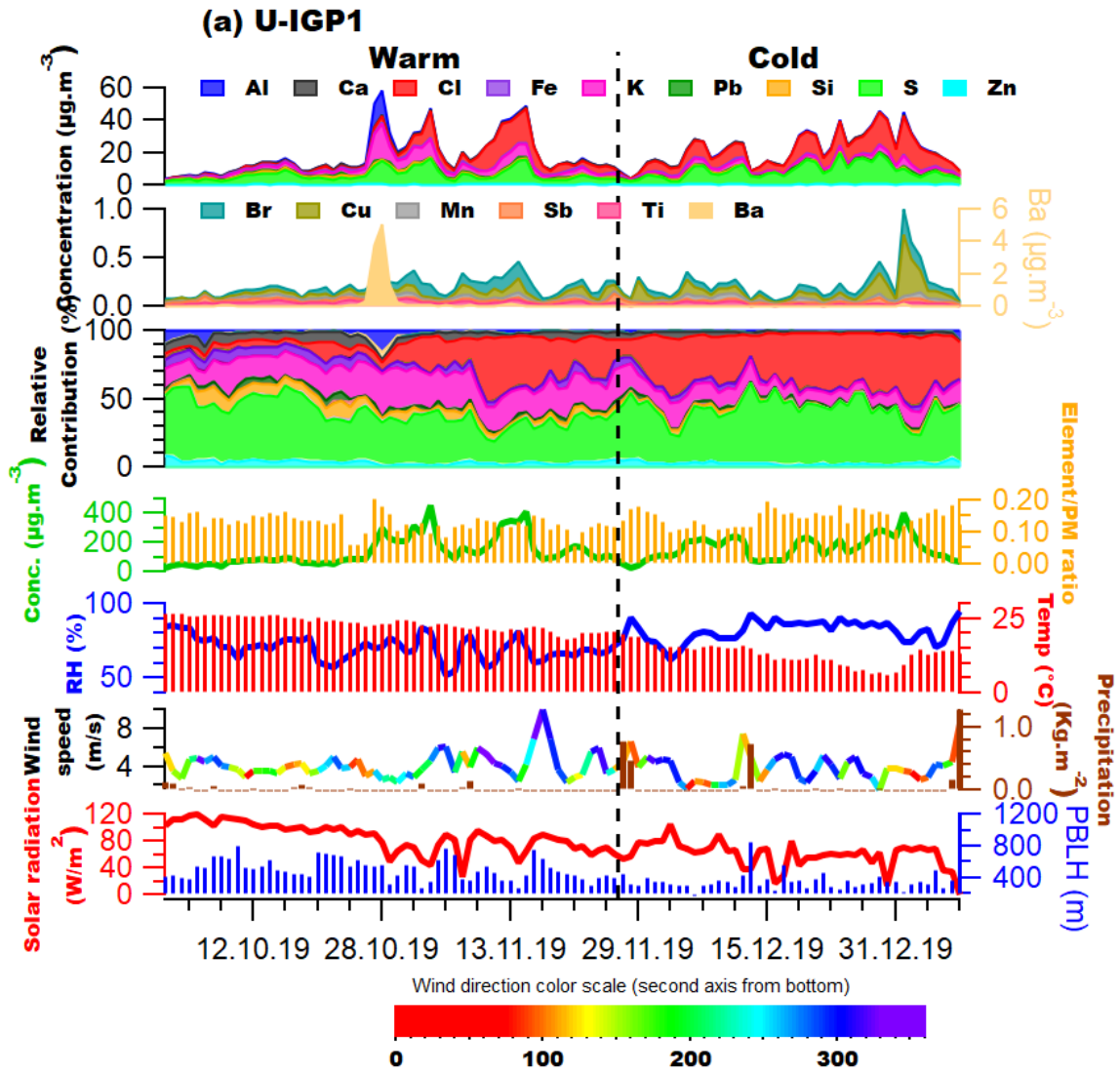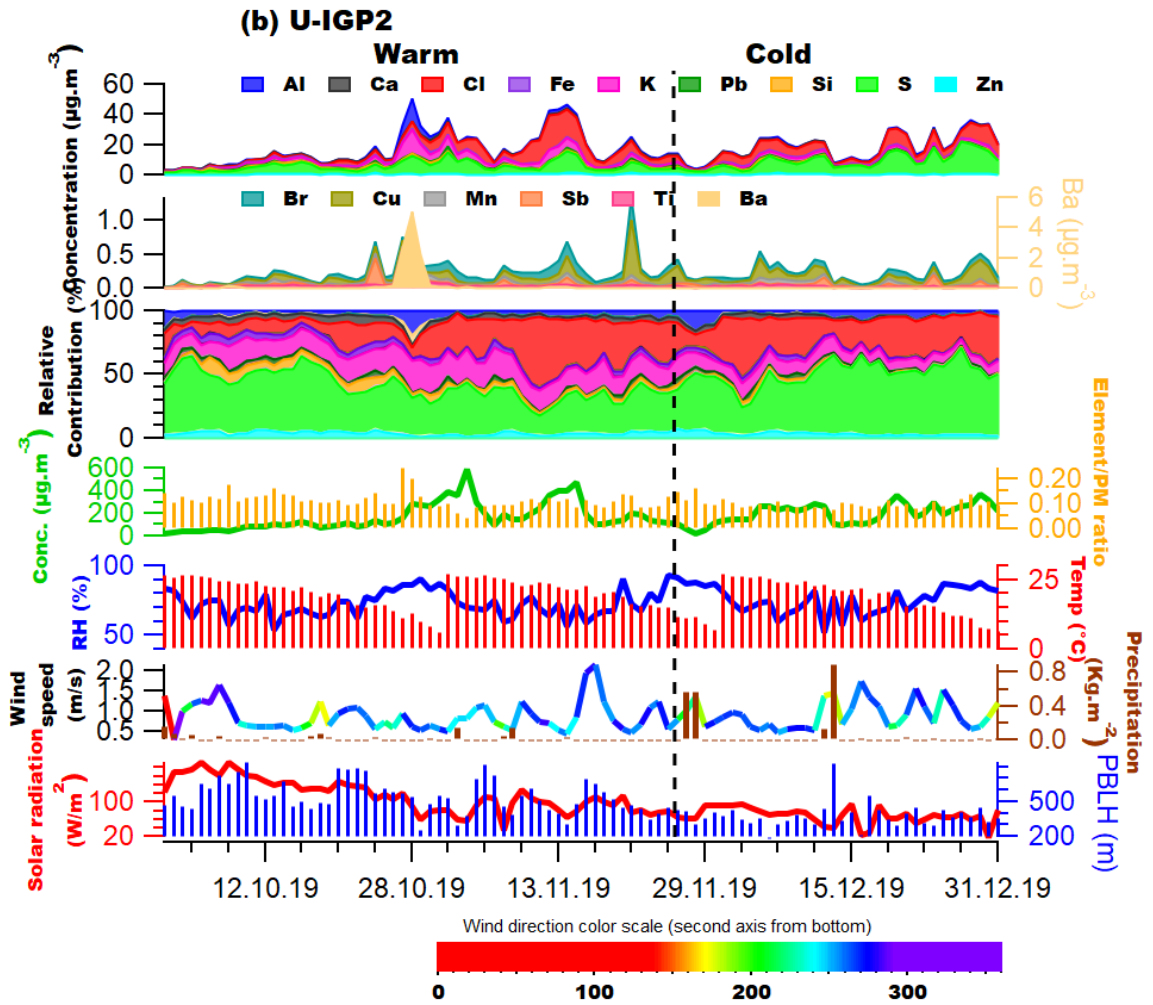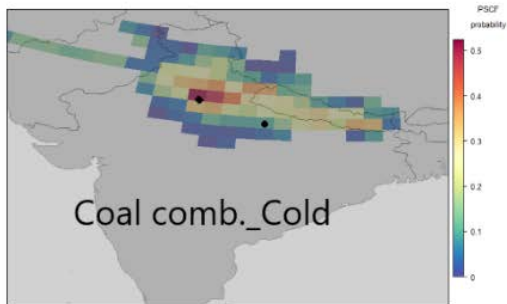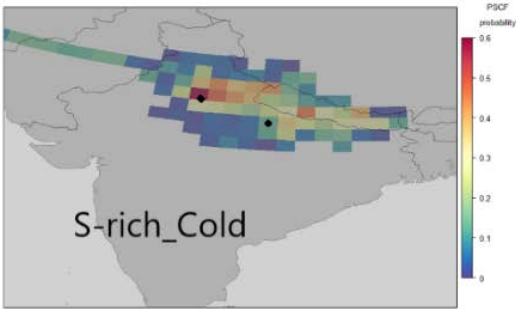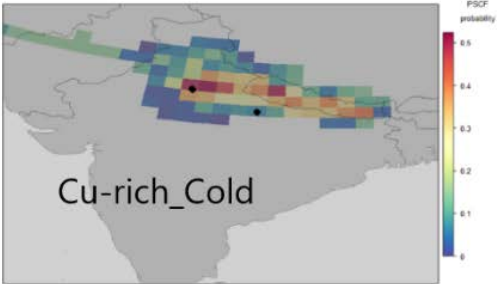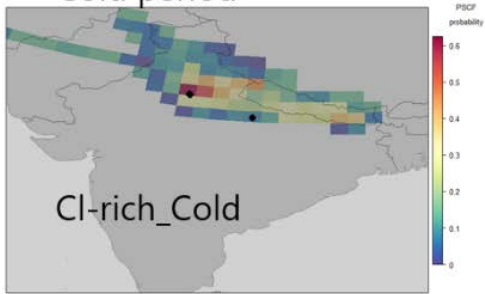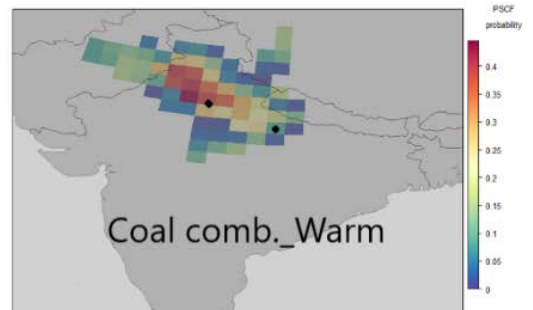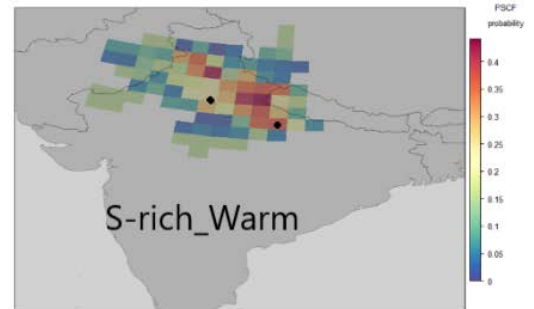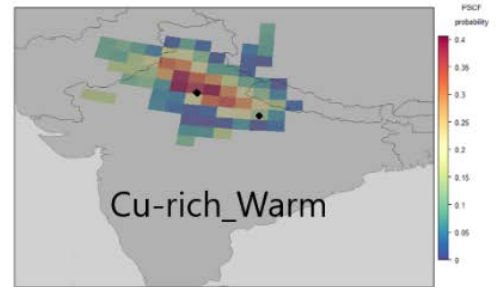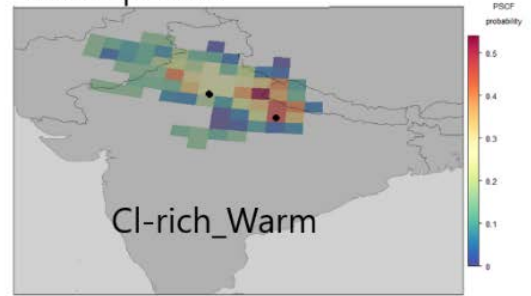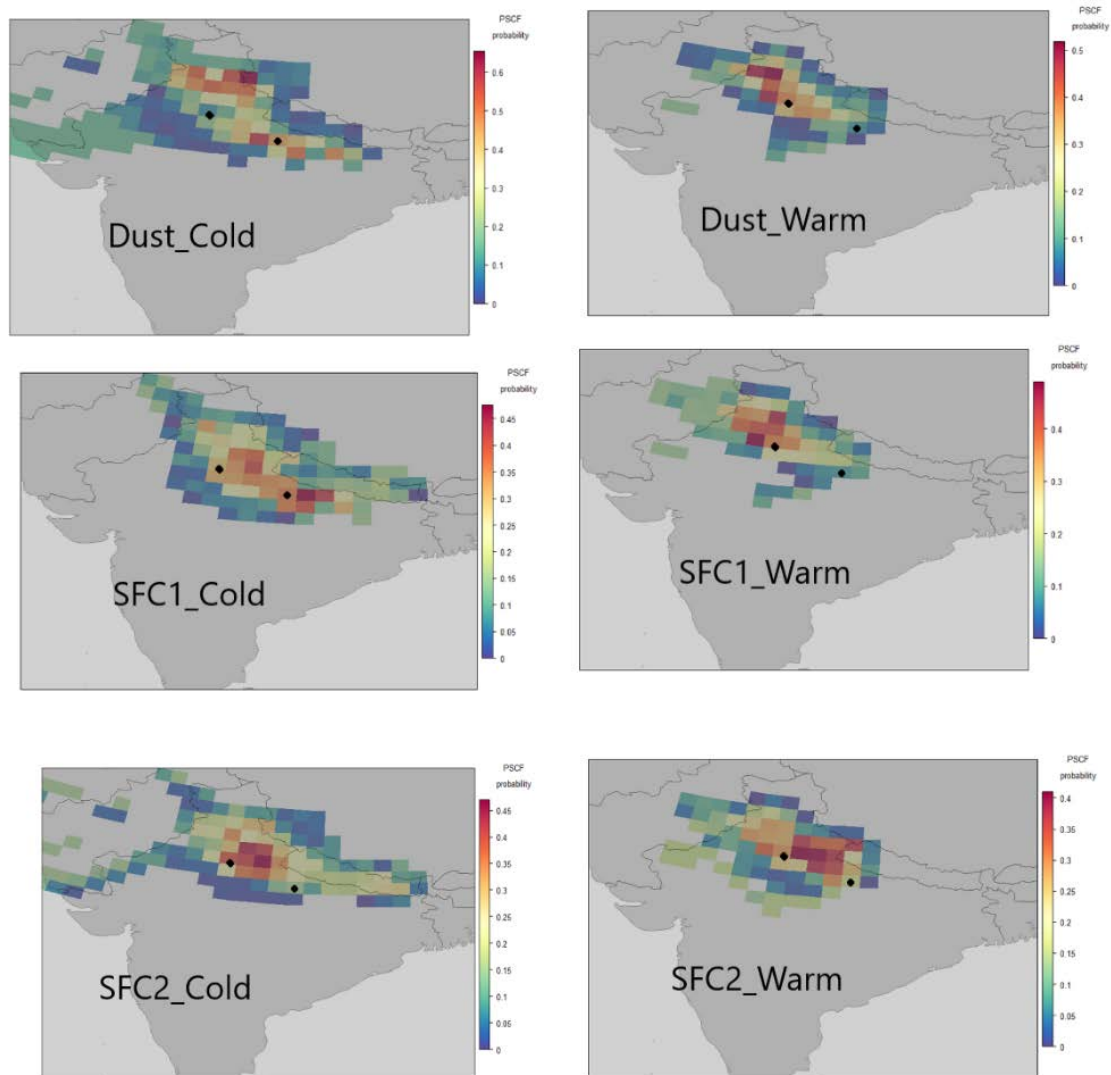
Figure S4. PSCF plot for multi-site (using three IGP sites elemental sources data) for the warm and cold period of the elemental sources
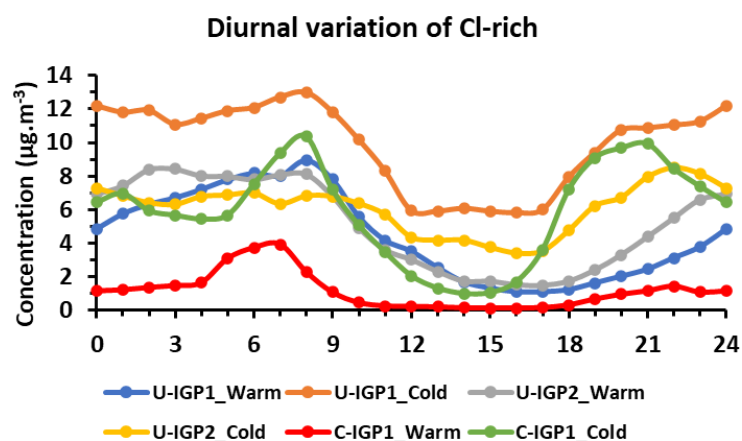
Figure S5. Diurnal variation of Cl-rich source during both warm and cold periods and at all the three sites

S1. Selection of optimum elemental ME-2 solution

The unconstrained Positive Matrix Factorization (PMF) was applied to the sub-hourly elemental dataset at all three sites, ranging from three to eleven factors. The initial step in the solution selection process involved determining the minimum number of factors for further investigation, focusing on the factor that exhibited the maximum change in the Q/Qexp value. Specifically, at U-IGP1, a 37.9% change was observed at factor nb 7, while at U-IGP2 and C-IGP1, the changes were 28.3% and 22.2%, respectively, also at factor nb 7, as depicted in graph S3. Consequently, the minimum number of factors for subsequent investigation was determined to be seven.

At the U-IGP1 site, the 7-factor solution successfully distinguished Pb-rich, Cu-rich, Cl-rich, and S-rich sources. However, SFC2 exhibited a mixture with Al (which displayed a strong correlation with K, Sr, and Ba, as shown in Fig.S1, elements associated with fireworks), and SFC1 was mixed with Si (which showed a good correlation with Ca and other dust-related elements), as well as one Ca-rich dust factor. Upon transitioning to the 8-factor solution, an additional dust factor was resolved, but the S-rich factor remained mixed, similar to the 7-factor solution. To assess the stability of factor profiles, the 8-factor solution was executed with ten different seeds. It was discovered that the primary cause of mixing was the transition of Al and Si from one factor to another (Al was part of SFC1 in the 7-factor solution but appeared in the S-rich factor in the 8-factor solution). Therefore, the clean fireworks factor with Al was derived from the 10-factor solution and incorporated into the 8-factor solution. The fireworks factor profile was constrained with the a-value ranging from 0 to 1, in increments of 0.1. Ultimately, an a-value of 0.2 was determined to be the optimal solution. However, SFC1 still exhibited mixing, so its profile was constrained as well. Consequently, a solution with a=0.2 for fireworks and a=0.1 for SFC1 was selected as the environmentally reasonable solution based on the Understanding Explained Variance (UEV), physical interpretation of factors, time series, correlation with external tracers, and diurnal variation. The correlation of elements among themselves also helped in selection of factors as shown in Fig. S1. To evaluate the reproducibility of the 8-factor solution with a=0.2 for fireworks and a=0.1 for SFC1, ten seed runs were conducted. The solution was deemed optimal, with a variation in

Q/Qexp of less than 2.3% at U-IGP1. Bootstrapping was performed on the final solution, and a detailed discussion of the results can be found in section S2.

At the U-IGP2 site, in the 7-factor solution, the sulfur-rich component was mixed with aluminum, and SFC1 was also combined due to its contributions from crustal elements. Moving on to the 8-factor solution, the silicon from the dust factor was mixed with SFC1, as well as chromium, manganese, nickel, and iron, which were previously associated with dust. However, these elements were separated. Similar to the U-IGP1 site, the fireworks during Diwali caused issues. When the unconstrained 8-factor solution was run with 10 different initializations, elements such as aluminum, silicon, and other dust-related components could not be cleanly resolved and were getting mixed with other factor profiles. Consequently, to obtain a cleaner fireworks factor, it was constrained in the 8-factor solution. The fireworks profile was constrained using an 'a-value' ranging from 0 to 1, with a step size of 0.1. After considering factors such as the unexplained variance (UEV), physical interpretation, time series, correlation with external tracers, and diurnal fluctuations, the solution with an 'a-value' of 0.4 for fireworks was selected as the most environmentally appropriate. To assess the reproducibility of the 8-factor solution with an 'a-value' of 0.4 for fireworks, ten runs were performed with different random seeds. The solution was considered the best one when the variance in Q/Qexp was less than 0.01% at U-IGP2 (Fig. S8 (a)). Finally, bootstrapping was conducted on the final solution, and the detailed results are discussed in section S2.

At the C-IGP1 site, in the 7-factor solution, the following factors were resolved without any mixing: chlorine-rich, sulfur-rich, SFC1, SFC2, copper-rich, coal combustion, and dust. When moving to the 8-factor solution, the dust factor split into two components, one dominated by potassium, calcium, and iron, and the other dominated by aluminum and silicon. However, when observing the time series of the two dust factors, similar peaks were observed (Fig. S3 (b)), and there was a strong correlation between silicon and calcium as shown in Fig. 1(c), which did not support the separation of the two dust factors. To further confirm this, an attempt was made to constrain the high potassium signal in one of the dust factors, but no sufficient evidence was found to justify separate dust factors. After conducting a thorough investigation considering physical interpretability, diurnal patterns, time series, and residuals, it was determined that the seven-factor solution was the most environmentally viable option.

To evaluate the reproducibility of the seven-factor solution, ten preliminary runs with random initializations were performed. The solution was considered optimal when the variation in Q/Qexp at C-IGP1 was less than 10.3% (Fig. S8 (a)). Bootstrapping was then applied to the final solution, and the detailed results are discussed in section S2.
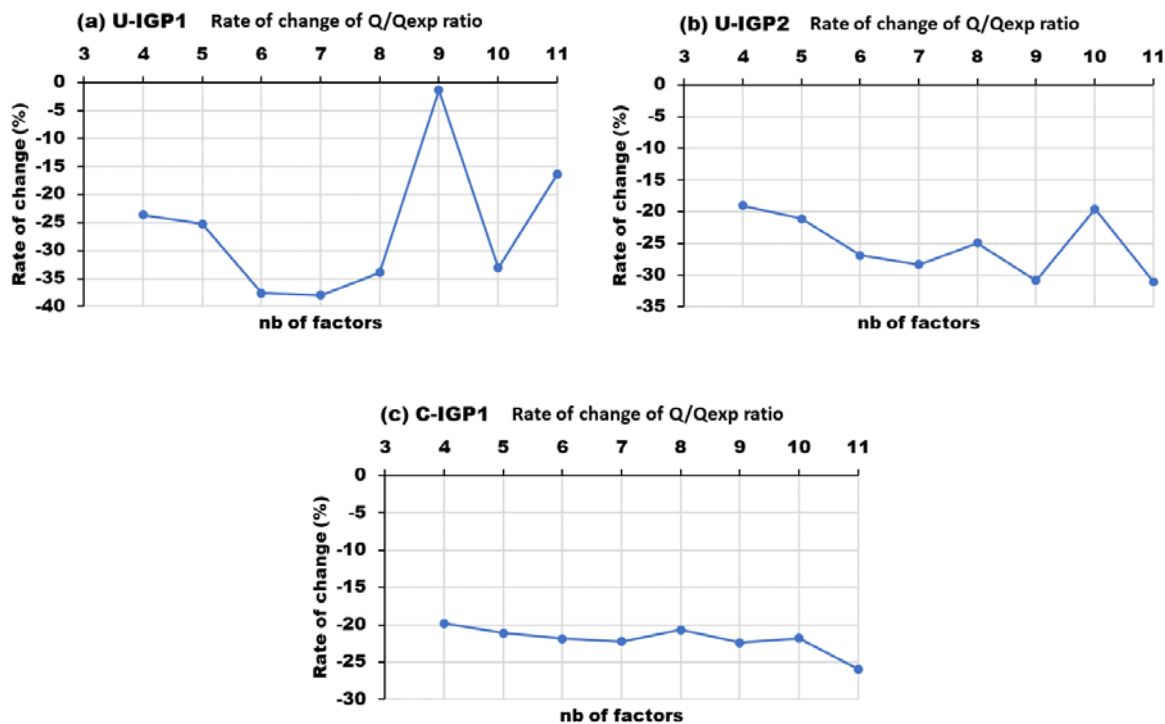
Figure S6. Relative percentage change in Q/Q$_{exp}$ ratio for the unconstrained PMF run from 3-factor to 11-factor solution at site (a) U-IGP1 (b) U-IGP2 and (c) C-IGP1.
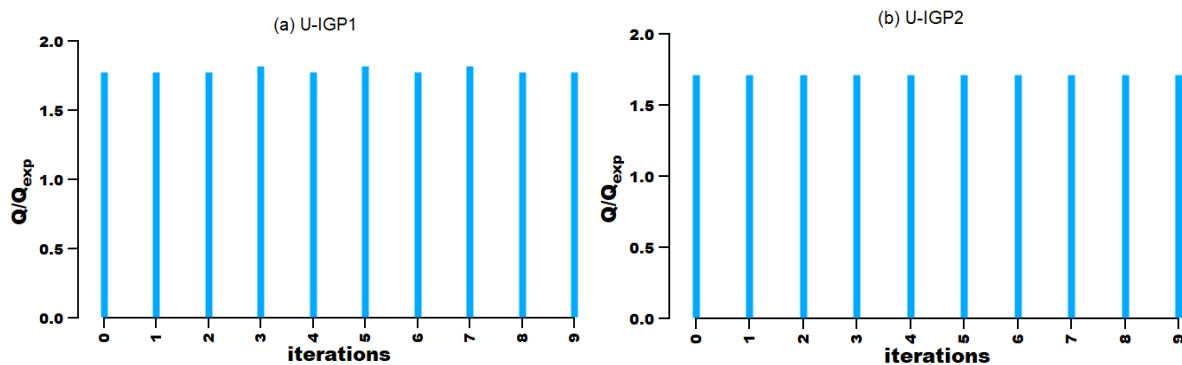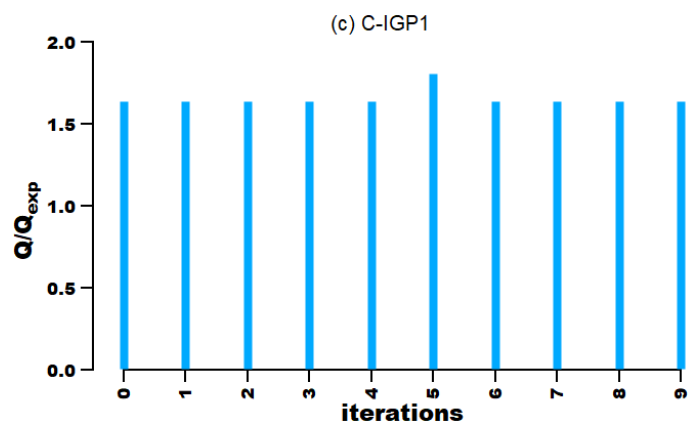
Figure S7. For elemental unconstrained PMF factors, the variation in Q/Qexp for 10 seeds (a) U-IGP1, (b) U-IGP2 and (c) C-IGP1.
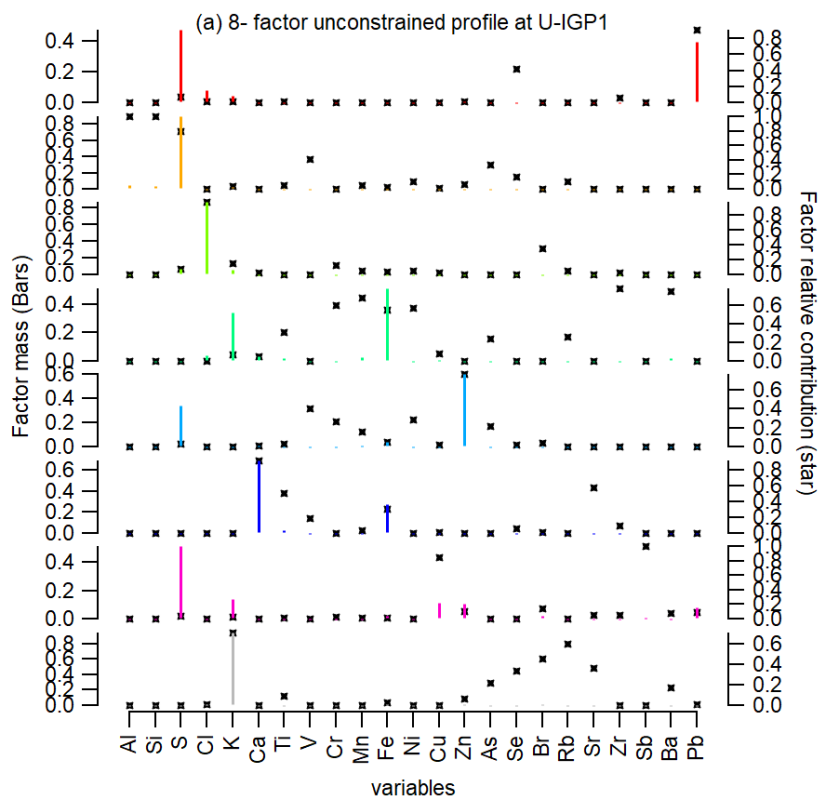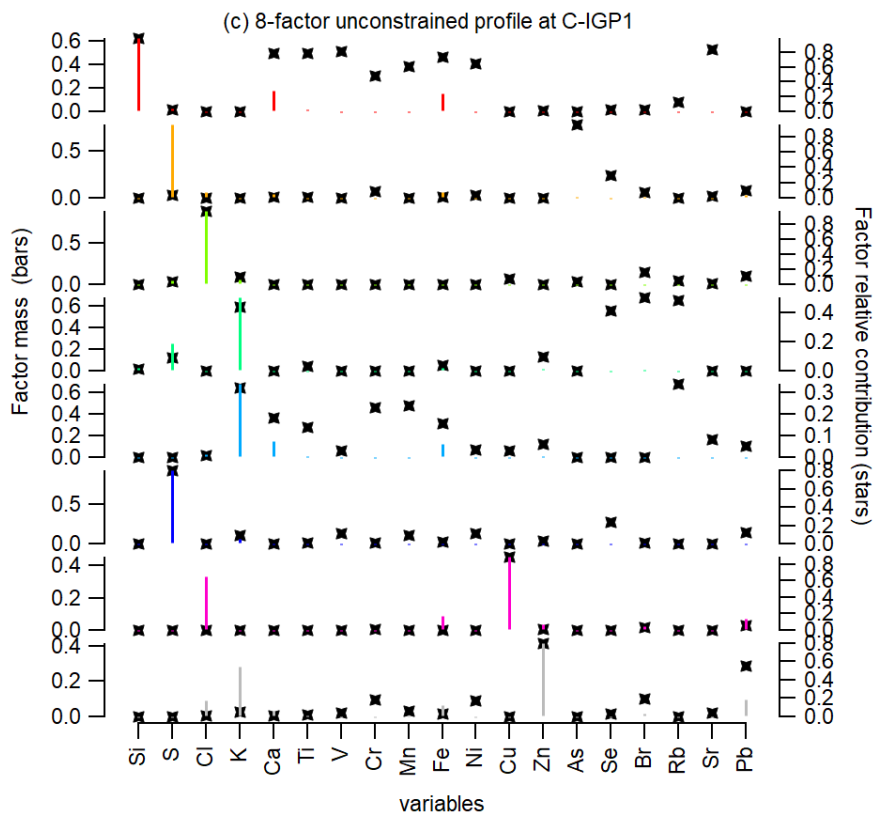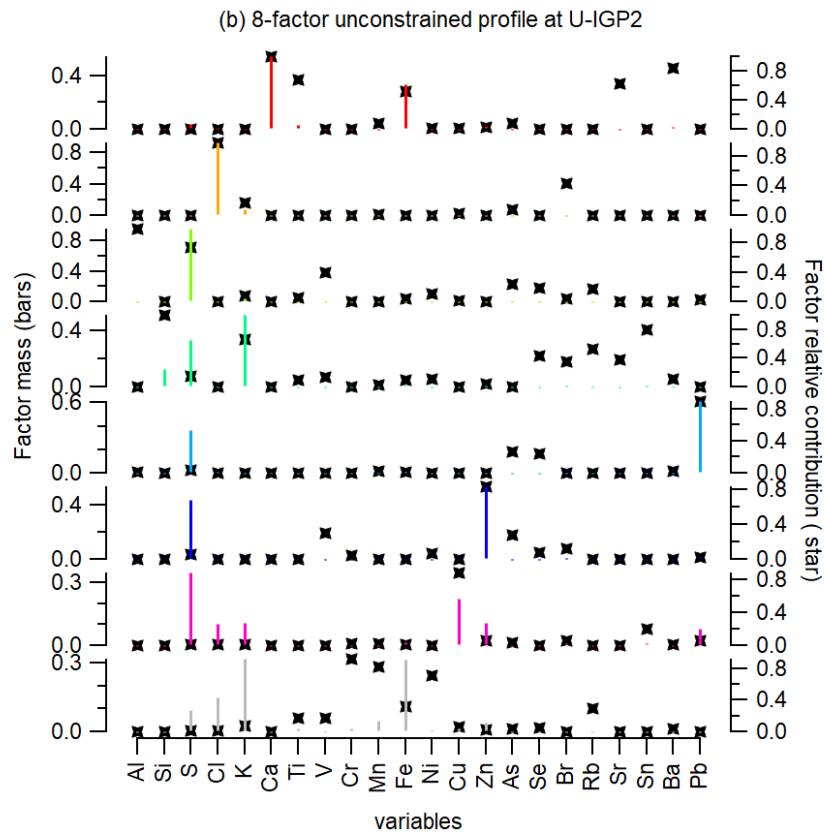
Figure S8. The source profile of the 8-factor unconstrained solution used in the analysis while selecting the final number of factors at (a) U-IGP1, (b) U-IGP2 and (c) C-IGP1.
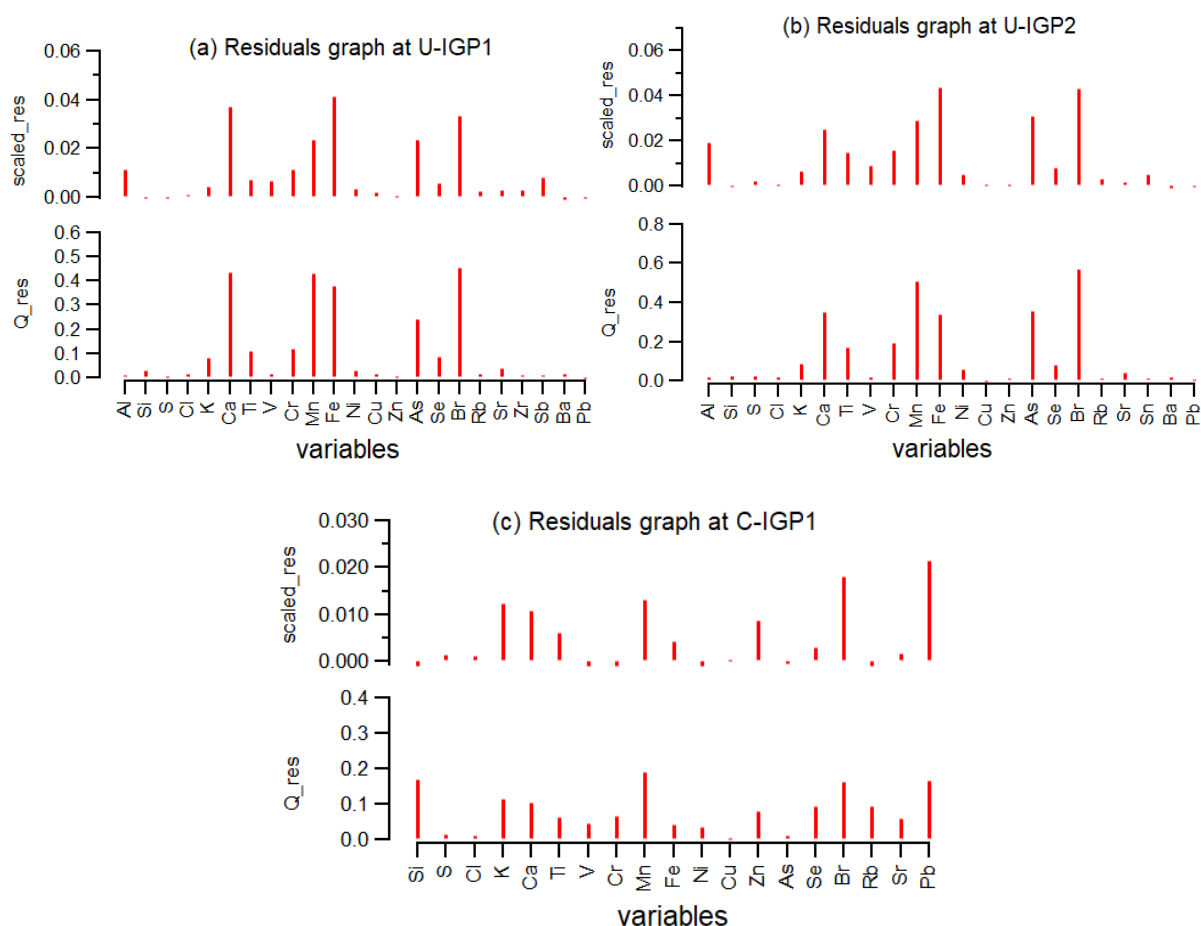
Figure S9. The variation of Q_reisdual and scaled_residual for each elemental species at (a) U-IGP1, (b) U-IGP2 and (c) C-IGP1 sites.

S2. Description of final selected elemental ME-2 solution

The 7 factors Cl-rich, S-rich, Cu-rich, Coal combustion, SFC1, SFC2 and dust related sources are resolved at all the three sites, while an additional fireworks factor was resolved at the U-IGP1 and U-IGP2 sites. The seven factors resolved at all three sites are Cl-rich, S-rich, Cu-rich, Coal combustion, SFC1, SFC2, and dust-related sources. Additionally, a fireworks factor was identified at the U-IGP1 and U-IGP2 sites. Our study focuses on the variation of these seven common factors, which will be further discussed in the section describing factor profiles. The role of meteorology in the variation of elemental sources between the three sites in the IGP region is also investigated. It is important to note that a separate study on the fireworks factor during Diwali at two sites in the U-IGP was already conducted by Manchanda et al. (2022).

The Cl-rich factor profile mass (U-IGP1, U-IGP2, and C-IGP1) is primarily dominated by high levels of Cl (93%, 94%, and 87%). It also exhibits relative contributions from Br (30%, 38%, and 17%) and

K (12%, 13%, and 16%), which are markers for combustion related to trash burning (specifically plastic/PVC) and brick kilns. A source apportionment study by Wang et al. (2022) investigated the composition of the Cl-rich factor and identified contributions from combustion processes, such as trash burning and brick kilns. Their findings support that the Cl-rich factor is predominantly influenced by emissions from these combustion-related sources. The good correlation (R=0.6-0.7) of Cl-rich with PAHs indicates incomplete combustion of plastic/PVC products mixed with other waste materials, especially from waste incineration. Jin et al. (2020) found that waste combustion and metallurgical smelting are the primary anthropogenic sources of chlorinated and brominated PAH emissions. Additionally, e-waste dismantling has been suggested as an emerging source of chlorinated PAHs.

The S-rich factor mass primarily consists of high signals from S (98%, 98%, and 88%). It also shows relative contributions from Se (20%, 17%, and 32%) and V (29%, 44%, and 12%). These elements are associated with fly ash from coal combustion in thermal power plants. Li et al. (2022) conducted a source apportionment analysis on the S-rich factor and reported a strong association with fly ash emissions from coal combustion. The presence of selenium and vanadium in the S-rich factor, as identified in their study, provides additional evidence linking this factor to coal combustion sources. The S-rich factor demonstrates a good correlation with CO_2 (R=0.65) at all three sites, indicating its aged nature. The diurnal peak during the afternoon suggests that it undergoes transport. The Cu-rich source exhibits a very high relative contribution of Cu (90%, 91%, and 91%) along with Pb (9%, 5%, and 5%) and Br (16%, 8%, and 2%). Cu and Pb are related to industrial metal sources, lead-acid battery recycling, and burning of electrical/electronic waste containing Cu (such as cables and circuit boards). Chen et al. (2022) conducted a source apportionment analysis and found that the high levels of lead and copper in the Cu-rich factor can be attributed to industrial emissions, particularly from metal-related industries and lead-acid battery recycling. This finding aligns with the hypothesis that the Cu-rich factor is influenced by industrial metal sources.

The coal combustion factor is characterized by high signals of S (46%, 48%, and 39%) and Pb (36%, 44%, and 3.4%). It also shows significant relative contributions from Pb (90%, 86%, and 10%), As (1%, 26%, and 94%), and Se (40%, 24%, and 29%). These elements indicate emissions from industrial and domestic coal combustion, as well as from lead smelting. As and Se are commonly used as markers

for coal combustion, and lead in coal is mainly present in the form of sulfides (e.g., galena and pyrite) (Cui et al., 2019). Zhang et al. (2023), the coal combustion factor was found to be dominated by sulfur and lead, confirming the presence of emissions from coal combustion sources. The identification of arsenic and selenium in the coal combustion factor further supports that these elements serve as markers for industrial/domestic coal combustion activities and lead smelting emissions. The SFC1 factor profile mass (U-IGP1, U-IGP2, and C-IGP1) is mainly dominated by high signals of K (67%, 55%, and 64%), followed by S (32%, 41%, and 26%). It also exhibits high relative contributions from K (62%, 64%, and 49%), Rb (66%, 65%, and 55%), Br (49%, 43%, and 49%), and Se (34%, 46%, and 39%). The good correlation with PAHs (R=0.5-0.7) and the presence of these elements indicate that the SFC1 factor is associated with biomass burning, especially crop residue burning. In a recent source apportionment analysis conducted by Liu et al. (2023), the SFC1 factor was found to be strongly associated with biomass burning, particularly crop residue burning. The high levels of potassium and sulfur, as well as the correlation with PAHs, observed in their study provide additional evidence linking the SFC1 factor to biomass burning sources.

The SFC2 factor is characterized by a high relative contribution of Zn (83%, 85%, and 70%), Cr (27%, 26%, and 16%), and Ni (30%, 18%, and 15%). The presence of Zn, Cr, and Ni indicates the role of industrial waste burning (Rai et al., 2020). Investigating the SFC2 factor, a source apportionment study by Sharma et al. (2022) revealed significant contributions from industrial waste burning sources. The elevated levels of zinc, chromium, and nickel identified in their analysis support the hypothesis that the SFC2 factor is influenced by emissions from such industrial waste burning activities. The dust factor profile consists of mass from Si (32%, 32%, and 57%), Ca (26%, 24%, and 19%), and Fe (28%, 24%, and 19%). It also demonstrates high relative contributions from Si (97%, 96%, and 100%), Ca (90%, 98%, and 88%), Fe (80%, 78%, and 80%), Ti (74%, 83%, and 84%), Ni (47%, 57%, and 67%), Cr (50%, 64%, and 61%), and Mn (65%, 66%, and 71%). All these elements are related to dust sources, and they exhibit a very high correlation with each other, as shown in Fig. S1.
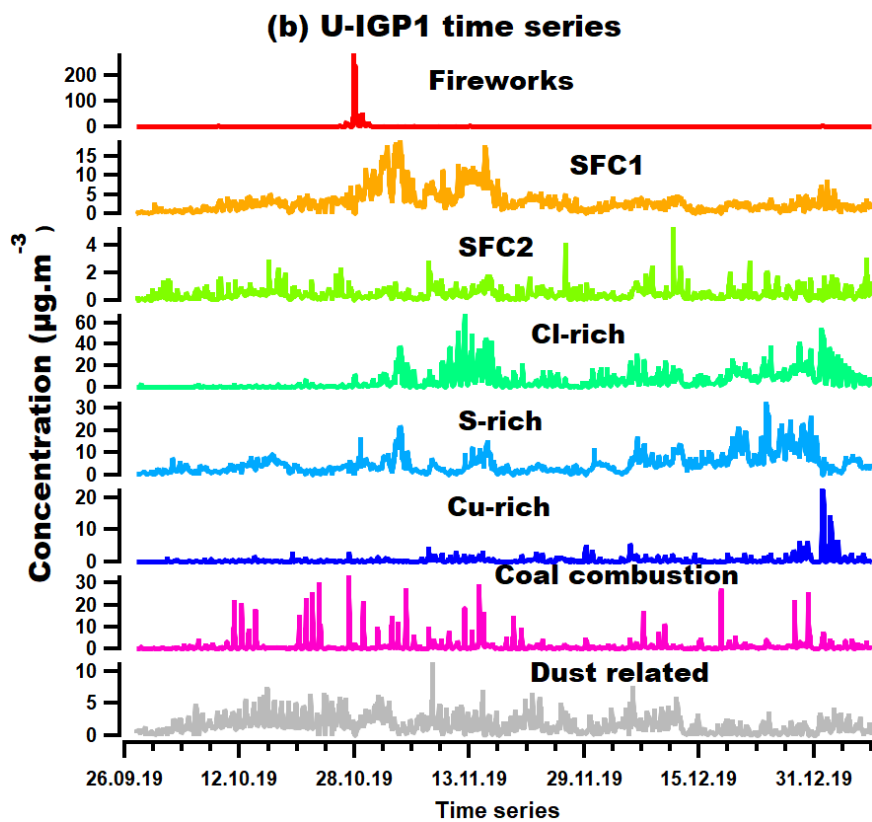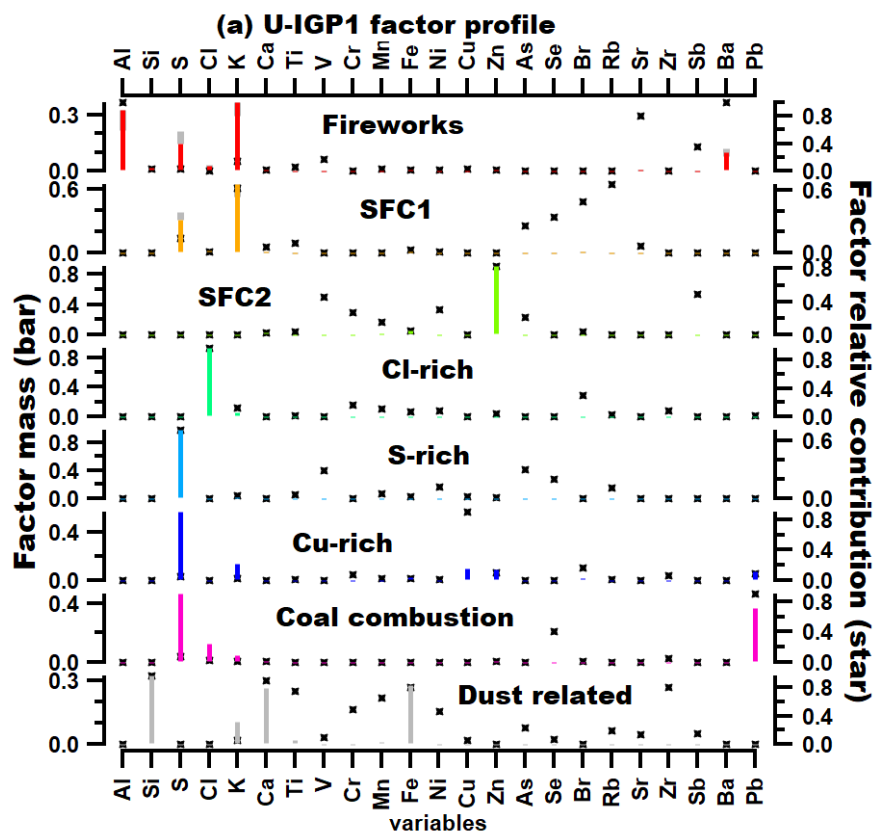
Figure S10. (a) Source profile of the 8-factor solution and (b) time series of the sources from the elemental source apportionment at U-IGP1.
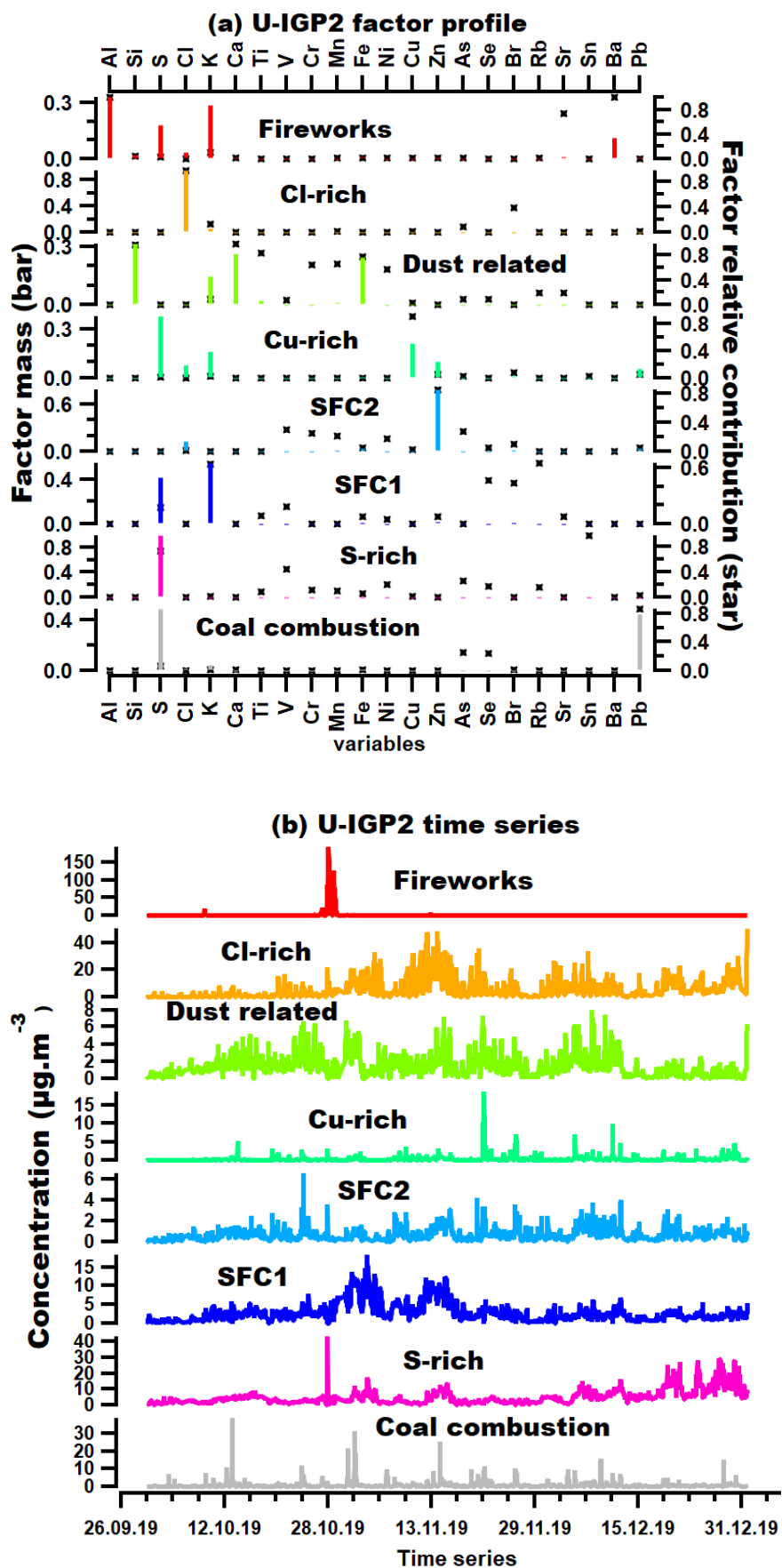
Figure S11. (a) Source profile of the 8-factor solution and (b) time series of the sources from the elemental source apportionment at U-IGP2.
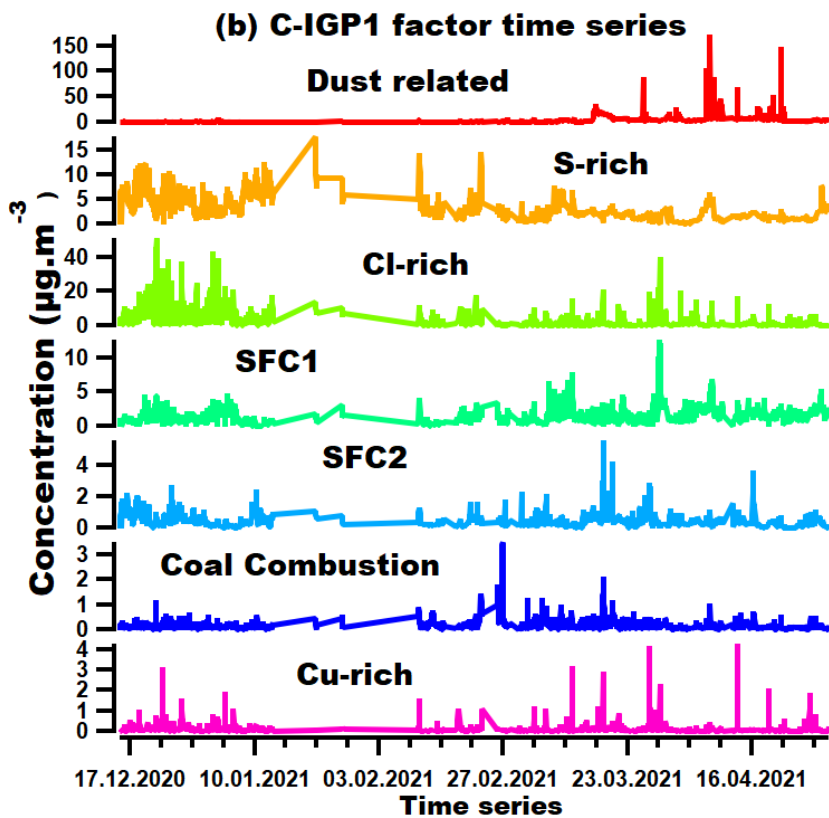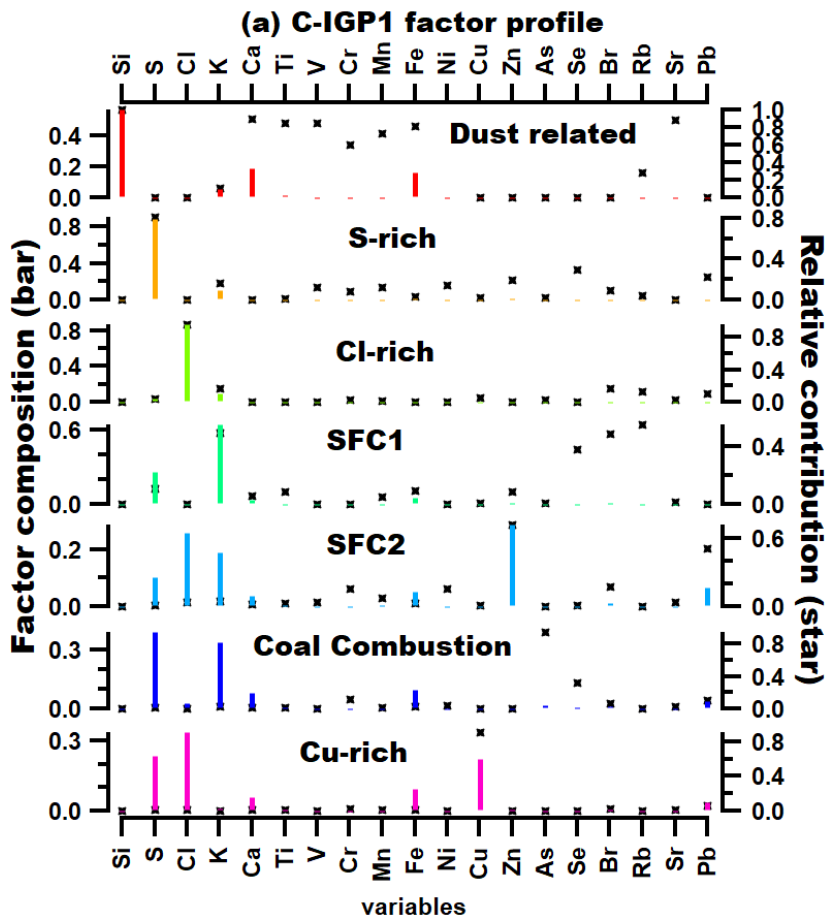
Figure S12. (a) Source profile of the 7-factor solution and (b) time series of the sources from the elemental source apportionment at C-IGP1.

(a) Heatmap for correlation of sources at U-IGP1 with elements
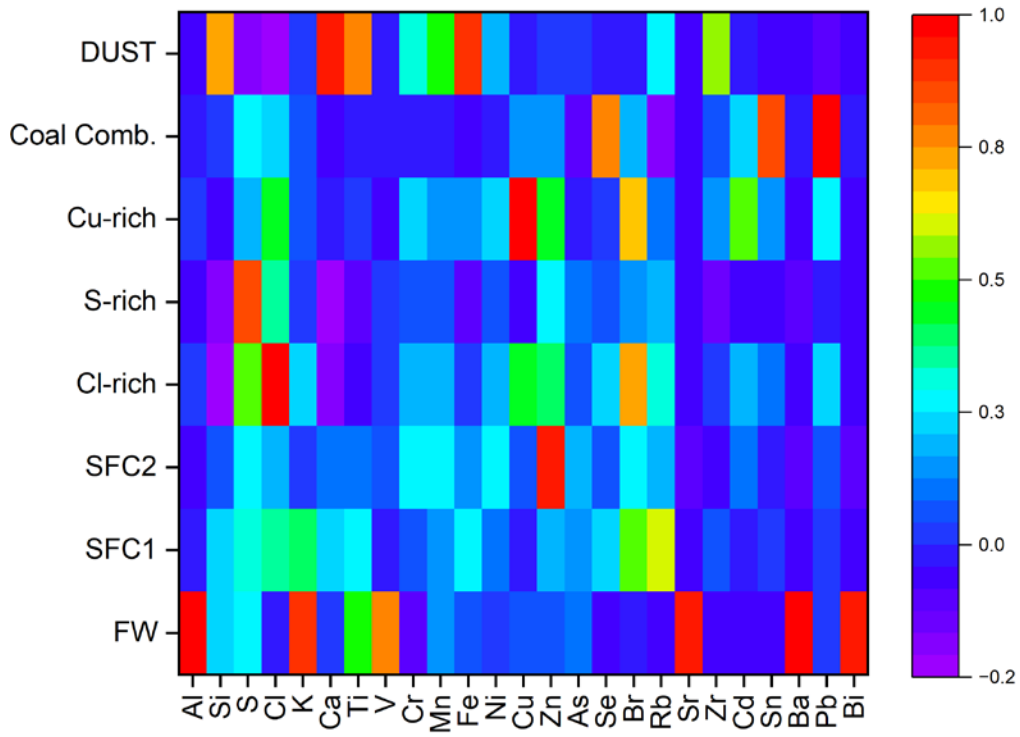
(b) Heatmap for correlation of sources at U-IGP1 with AMS markers, Meteorological markers and BC
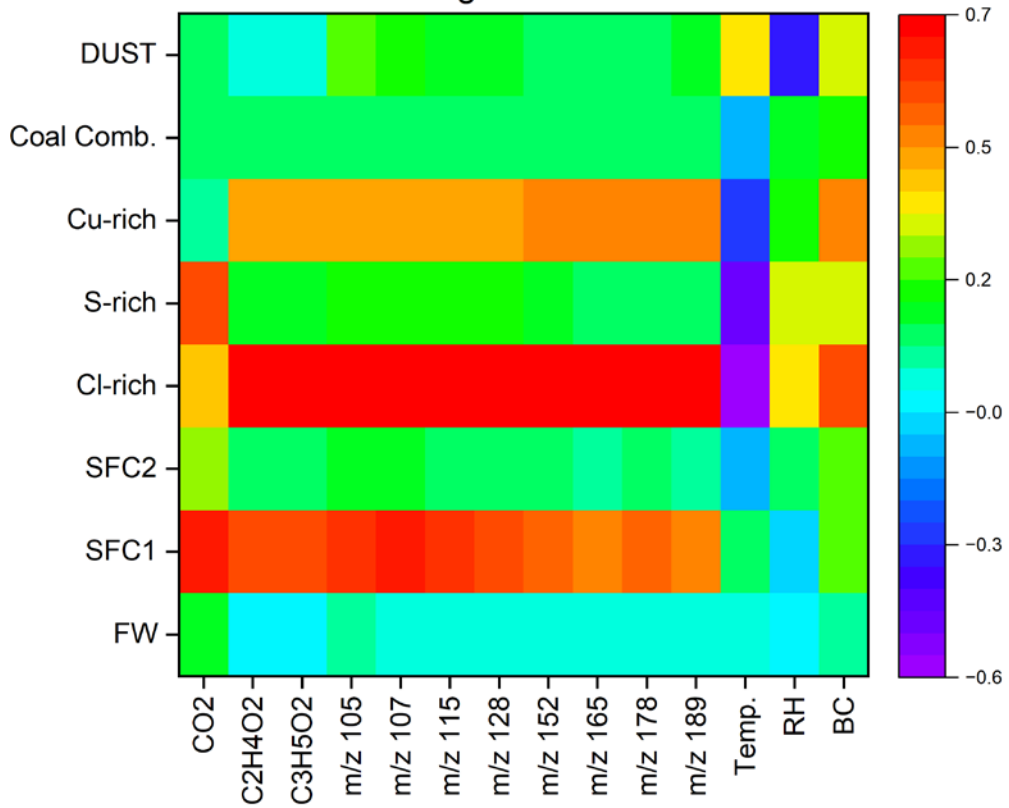
(c) Heatmap for correlation of sources at C-IGP1 with elements

(d) Heatmap for correlation of sources at U-IGP1 with AMS markers, Meteorological markers and BC
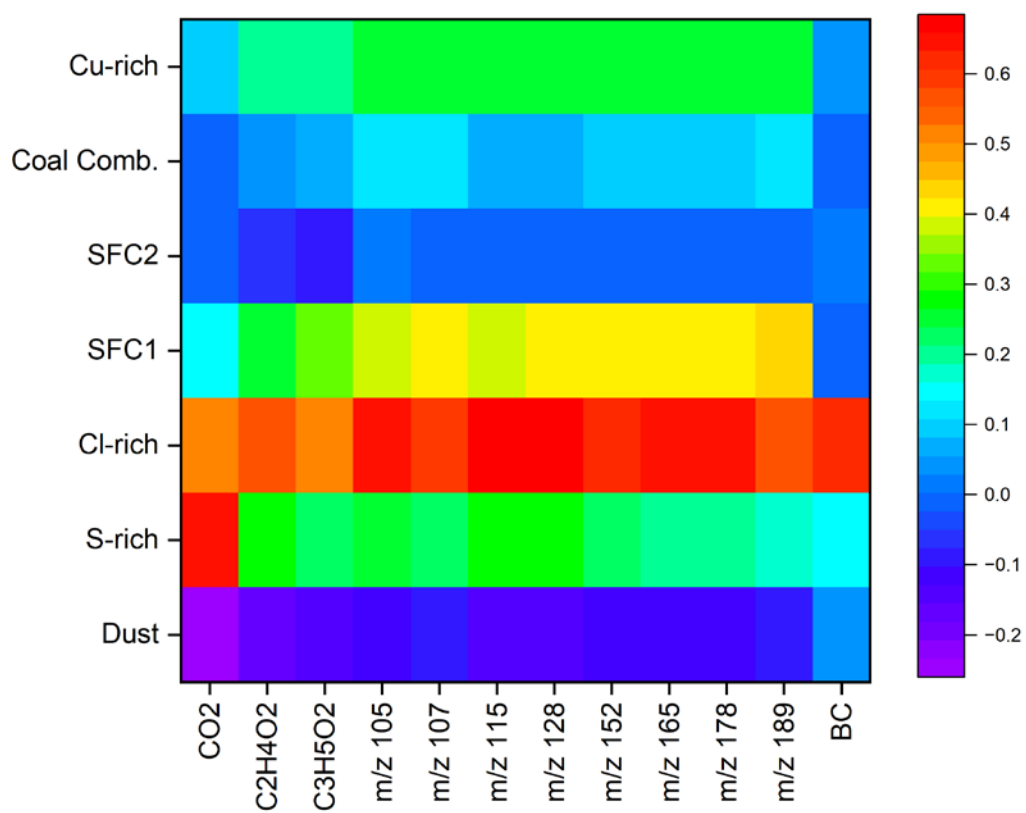
Figure S13. Heatmap showing correlation of resolved elemental sources with external tracers (a-f)

S3. Bootstrap analysis of the ME-2 results of OA and elements.

The bootstrap analysis was employed to assess the extent of factor mixing and to determine the specific factors involved in the mixing process. The methodology used in this analysis followed the approach described by Rai et al. (2020) and Stefenelli et al. (2019). For the elemental ME-2 results, the bootstrap analysis was conducted for the 8-factor solution at the U-IGP1 site, with constraints applied to the fireworks factor and SFC1 factor. At the U-IGP2 site, only the fireworks factor was constrained. At the C-IGP1 site, the final unconstrained 7-factor solution served as the base case. The a-value was randomly initialized within the range of 0 to 1, with an increment of 0.1. Out of the 500 bootstrap runs, 500 runs at the U-IGP1, 485 runs at the U-IGP2, and 448 runs at the C-IGP1 successfully passed the threshold criterion.

PMF runs that satisfied the acceptance criteria were retained to obtain the final results, leading to multiple repetitions for each time point (i). The variations observed among these iterations at each time point (i) can be used to assess rotational and statistical uncertainties. This study discusses both types of uncertainty, collectively referred to as PMF error (Canonaco et al., 2020). Other sources of uncertainty, such as anchor profile selection and the errors associated with criteria construction (e.g., type of criterion, tracer selection, and threshold determination), are not evaluated in this analysis but contribute to the overall uncertainty. In this investigation, the proposed relative PMF error in percentage is calculated using the following formula:

$$PMF_{error} = \frac{100}{2.n} \sum_{i=0}^{n} \left(\frac{\sigma}{avg}\right)_i$$

At the U-IGP1 site, the PMF errors for the factors were as follows: Cl-rich (1.5%), S-rich (1.5%), Cu-rich (4.5%), Coal combustion (4.8%), SFC1 (2.3%), SFC2 (4.5%), and dust (9%). At the U-IGP2 site, the PMF errors for the factors were Cl-rich (2%), S-rich (2.5%), Cu-rich (14%), Coal combustion (6%), SFC1 (7%), SFC2 (6%), and dust (10%). Finally, at the C-IGP1 site, the PMF errors for the factors were Cl-rich (3%), S-rich (4%), Cu-rich (26.5%), Coal combustion (32.5%), SFC1 (7%), SFC2 (14%), and dust (1%).

S4. Enrichment Factor (reference as Ti)

The enrichment of an element in comparison to its abundance in the upper continental crust (UCC) was assessed using EF analysis. Due to its stability and spatial homogeneity in the soil, Ti (Fomba et al., 2013; Majewski and Rogula-Kozowska, 2016; Wei et al., 1999) was chosen as the reference element for this investigation. The calculation of EFs and crustal contributions in elemental concentrations was done using the UCC composite model (Rudnik and Gao, 2014). The EF relative to Ti is provided for an element (X) in a sample is calculated by

$$\mathrm{EF} = \frac{\left(\frac{X}{Ti}\right) sample}{\left(\frac{X}{Ti}\right) crust}$$

For the initial evaluation of the impact of human-caused emissions on atmospheric elemental levels, the enrichment factor (EF) was calculated for each observed element, utilizing Ti as a reference element (Majewski and Rogula-Kozłowska, 2016; Fomba et al., 2013) and shown in Fig. 3 and 4. The comprehensive calculation and outcomes of the enrichment factor are expanded upon in supplementary section S4 and Table S1. The elements Al, Si, Fe, and Zr consistently exhibited EF values ranging from 0.4 to 2, indicating their association with crustal sources across all sites and periods. Conversely, the EF values for K, Cr, Mn, and Ni fell within the range of 2 to 20, suggesting a combined influence of both crustal and anthropogenic sources on these elements throughout all the sites and periods. On the other hand, the elements S, Cl, Cu, Zn, As, Se, Br, Cd, Sn, Sb, and Pb demonstrated EF values exceeding 20, indicating a significant anthropogenic impact on these elements. These findings will be utilized in the source apportionment section to further establish the links between these elements and their respective physical sources.
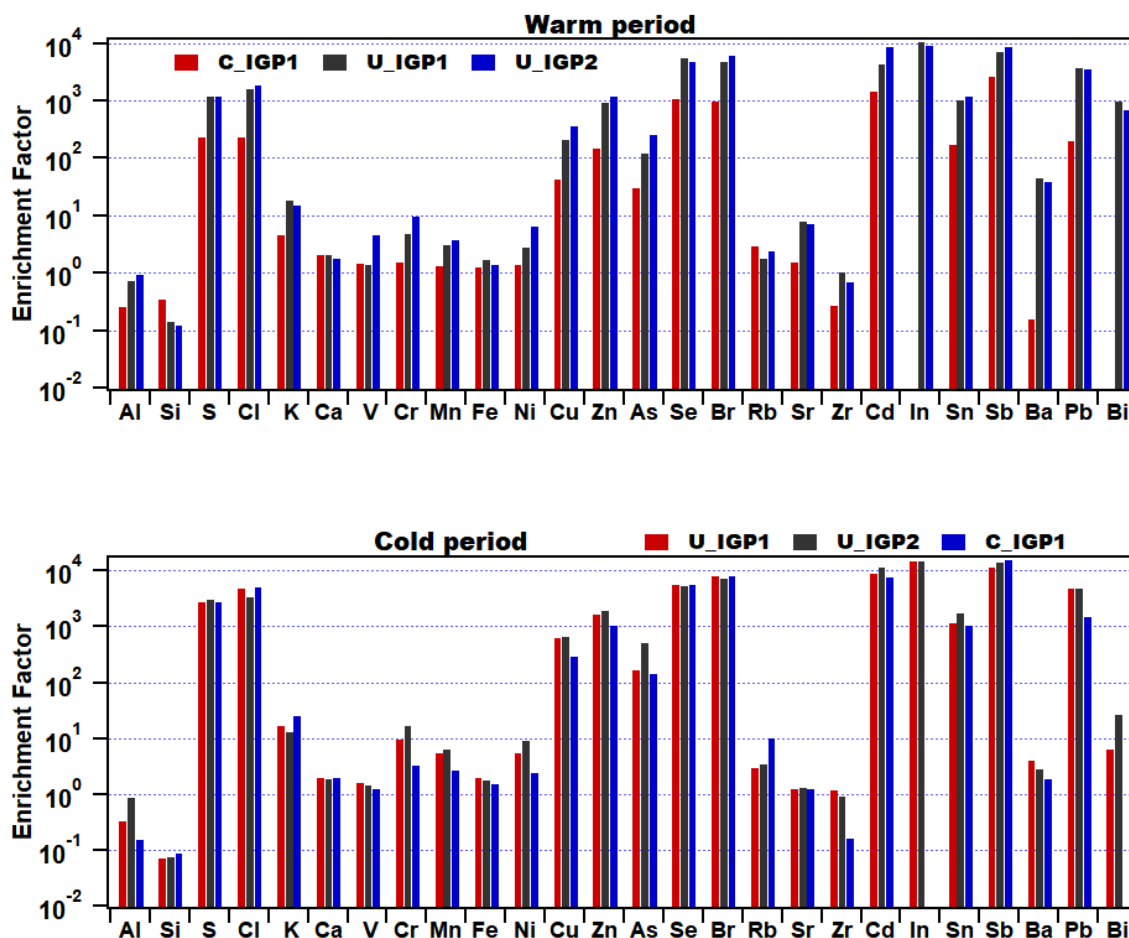
Figure S14. Enrichment factor of elements during cold period calculated using Ti as a reference at (a) U-IGP1 and (b) U-IGP2 and (c) C-IGP1 sites.

S5. Detailed discussion on diurnal variation of elemental sources

Furthermore, significant differences in diurnal patterns of sources were observed between warm and cold periods. The diurnal variation of SFC1 was higher in the warm period compared to the cold, attributed to crop-residue burning. Rice paddy-residue burning occurred in nearby states in the U-IGP region (October end), while wheat residue burning occurred in the C-IGP region (April-May) (Bray et al., 2019; Lan et al., 2022). Daytime SFC1 concentration was higher in the warm period, while favorable meteorological conditions during the cold period, such as low boundary layer height and calm wind speeds along with increased heating activities, led to higher nighttime concentrations. SFC2, associated with industrial waste burning, peaked early in the morning in both IGP regions during both periods (Fig. 6). Diurnal variation of SFC2 at the U-IGP2 exhibited distinct behavior, with high nighttime

concentrations (Fig. 6) attributed to proximity to industrial areas as discussed in our previous study by Shukla et al. 2023. Potential source regions of SFC2 showed minimal variation between warm and cold periods (Supplementary Fig. S4).
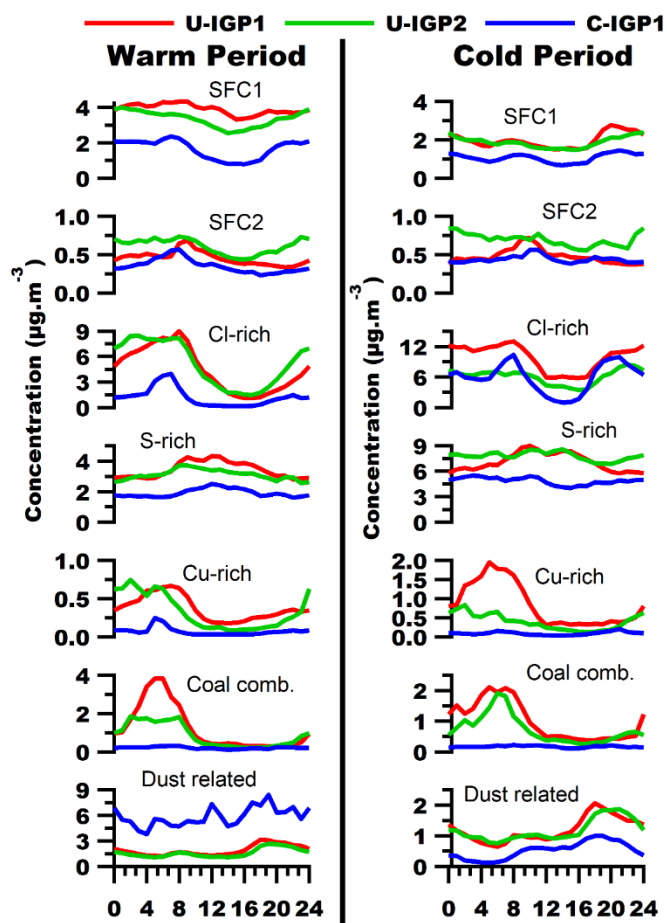
Figure S15. Diurnal variation of elemental sources at the three sites in the IGP region; U-IGP1, U-IGP2 and C-IGP1 during the warm and cold periods.

High chlorine concentrations in both IGP regions and periods peaked between 6:00 LT and 8:00 LT, attributed to the semi-volatile nature of ammonium chloride. This peak, accumulated during nighttime, converts to a gaseous form with rising temperatures. A distinct diurnal pattern in Cl-rich variation was observed between warm and cold periods (Fig. S5). During the warm period, Cl-rich concentrations began to increase around 8:00 PM, while during the cold period, they started to rise around 4:00 PM, likely due to differences in meteorological conditions. In the warm period, diurnal concentrations were similar at the U-IGP but markedly different from those at C-IGP, while during the cold period, significant differences were observed between the U-IGP locations, with U-IGP1 showing higher diurnal concentrations compared to U-IGP2 and C-IGP1. Additionally, in the cold period, an additional

nighttime peak, alongside the conventional morning peak, in Cl-rich variation was observed, contrasting with a single morning peak in both IGP regions during the warm period. During the warm period, both IGP regions showed high afternoon concentrations of S-rich source, with U-IGP1 having the highest, followed by U-IGP2 and C-IGP1 (Fig. 6). However, distinct diurnal patterns emerged during the cold period in both regions. U-IGP2 and C-IGP1 exhibited increased nighttime concentrations, suggesting potential sulfate formation via aqueous phase oxidation of SO2 by NO2 under high RH conditions. This phenomenon, reported by Lalchandani et al. (2022) in the U-IGP, contributes to new particle formation. Conversely, U-IGP1 displayed consistent high afternoon concentrations throughout both warm and cold periods. Notably, the S-rich source showed significant contributions near U-IGP during the cold period, while in the warm period, it shifted northwestward in the C-IGP region.

The Cu-rich source, mainly from industrial emissions, exhibited consistent diurnal patterns and concentrations from warm to cold periods at U-IGP2 (with two distinct peaks at 2:00 LT and 6:00 LT) and the C-IGP1 (a morning peak at 5:00 LT and during night at 21:00 LT) (Fig. 6). Conversely, U-IGP1 displayed distinct behavior during the transition, with peaks at 4:00 LT to 7:00 LT, showing higher concentrations during the cold period (0.67 µg.m−3 to 2 µg.m−3). The PSCF plot for Cu-rich source revealed proximity to U-IGP during the warm period, with additional northeast contribution during the cold period. Diurnal variation of coal combustion at U-IGP sites showed early morning peaks (5:00 LT to 7:00 LT) with higher peak at U-IGP1 during the warm period (~4 µg.m−3). In contrast, the diurnal variation of coal combustion at the C-IGP1 displayed two distinct high-concentration peaks during both day and night periods in both periods, unlike the single peak observed during the day in the U-IGP region. Coal combustion hotspot near U-IGP was evident during the cold period, whereas during the warm period, it was transported from northwest of U-IGP. Dust-related sources exhibited similar diurnal variations, with two peaks resembling rush traffic hours, except for a significant difference at C-IGP during warm period due to dust storms.

S6. Detailed discussion on spatial variation of elemental sources

During the warm period, the mean concentration of Cl-rich was higher at the U-IGP1 (9.83 µg.m−3) compared to U-IGP2 (6.03 µg.m−3). During the warm period, there was not much difference in the Cl-rich source concentration between the two sites during the daytime, but the difference increased more at the U-IGP2 at night (Fig.6). The mean concentration of the S-rich source was higher at the U-IGP2 (7.8 µg.m−3) compared to the other U-IGP2 (7.1 µg.m−3). At the U-IGP2, there was no difference in the mean concentration between day and night, but there was a significant difference in average concentrations between day and night (D/N=1.3). The average concentrations of Cu-rich and coal combustion were higher at the U-IGP1 (0.83 µg.m−3during warm and 0.99 µg.m−3 during cold) compared to U-IGP2 (0.39 µg.m−3 during warm and 0.71 µg.m−3 during cold). SFC2 and dust showed consistent concentrations at both sites. During the warm period at the C-IGP1, the RC of the dust source was 52% compared to 10.6-12% at the U-IGP sites. This significant difference was due to the occurrence of several high-concentration dust storms during the warm period sampling at the C-IGP1, while road dust resuspension was the primary contributor to the dust source at the U-IGP sites.
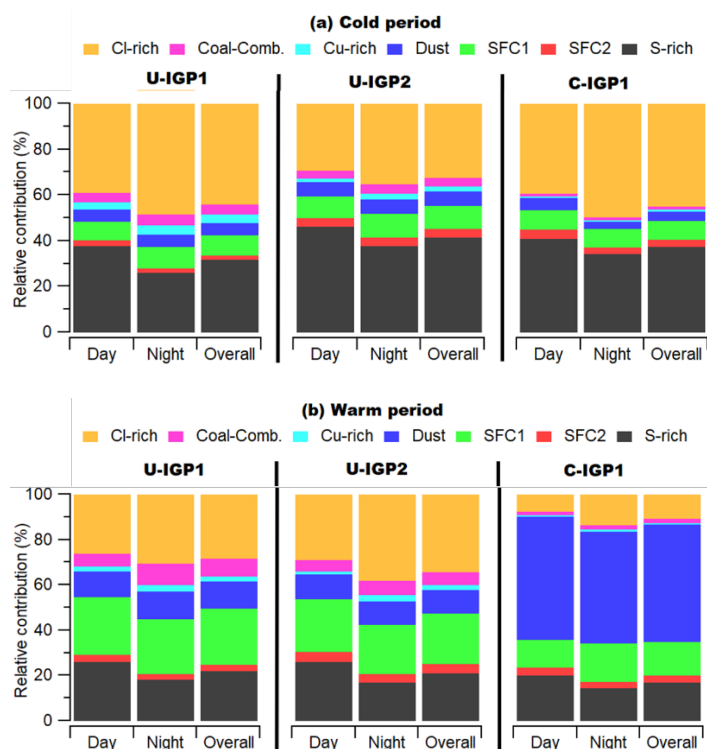
Figure S16. Variation in RC (%) of elemental sources at the three sites in the IGP region; U-IGP1, U-IGP2 and C-IGP1 between day, night and overall period during a) Cold and b) Warm.

S7. Variation of sources during clean periods in warm and cold

During both warm (C1) and cold (C2) clean episodes at both U-IGP sites, the average concentration of $PM_{2.5}$ remained relatively low, around 43 $\mu g.m^{-3}$. However, when considering the El-PM2.5, an interesting pattern emerged. U-IGP1 (15%) exhibited a almost similar elemental fraction as compared to U-IGP2 (12%) (summarized in Table S4). This suggests that different underlying factors influenced the composition of PM2.5 during these clean periods. In C1, characterized by higher solar ratio (SR) values of 112 at U-IGP1 and 170 at U-IGP2 (Fig. S3), the dominant elemental source was S-rich particles. This outcome can be attributed to the favorable conditions for the oxidation of SO2 through gas-phase reactions with OH, facilitated by the high PBLH of 501m at U-IGP1 and 571m at U-IGP2 (Table S4). The presence of S-rich particles in C1 shows that photochemical formation of sulfate dominated while also countering the dilution effects. In contrast, the major contributor during C2 was Cl-rich particles despite there were frequent precipitation during the C2 (Fig.S3). The low PBLH of approximately 350m at both U-IGP sites created a favorable environment for the accumulation of Cl-rich particles. Interestingly, the reduced SR values during the cold period (64 at U-IGP1 and 73 at U-IGP2) enabled the accumulation of chloride PM while preventing the conversion of particulate chloride into its gaseous phase, resulting in the sustained presence of Cl-rich particles in the atmosphere. At the C-IGP1, the PM2.5 average concentration during C1 was 31 $\mu g.m-3$, slightly lower than the U-IGP sites. However, during C2, the PM2.5 concentration notably increased to 52 $\mu g.m-3$. The elemental fraction exhibited a similar pattern, with 17% during C1 and 12% during C2 (Table S4), indicating variations in the composition of PM2.5 between the warm and cold periods at the C-IGP1.

During period C1 at all three sites, the S-rich and Dust sources were dominant (Fig. 8). However, during period C2, both S-rich and Cl-rich sources dominated in the IGP region across all three sites, highlighting the significant influence of meteorology and dynamic emission sources. We examined two distinct pollution episodes, namely EP1 and EP2, both occurring during the warm period. These episodes were characterized by a significant surge in $PM_{2.5}$ concentrations, indicating a notable increase in pollution levels. At U-IGP1, $PM_{2.5}$ concentrations multiplied by a factor of 6.7 (EP1) and 5.7 (EP2).

Similarly, U-IGP2 experienced an increase by a factor of 9 (EP1) and 7.3 (EP2), while C-IGP1 observed a factor of 2.9 increase for both episodes.

Table S1: Enrichment factor calculated using Ti as reference at U-IGP1, U-IGP2 and C-IGP1 sites.

		Warm	Cold
Group 1 (0.4 to 2)	U-IGP1	Al, Si, V, Fe, Rb and Zr	Al, Si, V, Sr and Zr
	U-IGP2	Al, Si, Ca, Fe and Zr	Al, Si, Ca, V, Fe, Sr and Zr
	C-IGP1	Al, Si, V, Cr, Mn, Fe, Ni, Sr, Zr and Ba	Al, Si, Ca, V, Fe, Sr, Zr and Ba
Group 2 (2 to 20):	U-IGP1	K, Ca,Cr,Mn,Ni and Sr	K, Ca,Cr,Mn,Fe,Ni,Rb,Ba and Bi
	U-IGP2	K, V,Cr,Mn,Ni,Rb and Sr	K, Cr, Mn, Ni, Rb and Ba
	C-IGP1	Cr,Mn,Ni and Rb	K, Ca and Rb
Group 3 (>20):	U-IGP1	S,Cl,Cu,Zn,As,Se,Br,Cd,In,Sn,Sb, Ba, Pb and Bi	S,Cl,Cu,Zn,As,Se,Br,Cd,In,Sn,Sb and Pb
	U-IGP2	S,Cl,Cu,Zn,As,Se,Br,Cd,In,Sn,Sb, Ba, Pb and Bi	S,Cl,Cu,Zn,As,Se,Br,Cd,In,Sn,Sb, Pb and Bi
	C-IGP1	S,Cl,Cu,Zn,As,Se,Br,Cd,Sn,Sb and Pb	S,Cl,K,Cu,Zn,As,Se,Br,Cd,Sn,Sb and Pb

*Group 1 (0.4 to 2): implies that these particles are associated with crustal sources

*Group 2 (2 to 20): implies that these are from mixed sources including crustal and anthropogenic

*Group 3 (>20): implies that they have a strong anthropogenic influence

Table S2: Xact mean concentration($\mu g.m^{-3}$), standard deviation (S.D), minimum and maximum values for 30 min sampling time at U-IGP1, U-IGP2 and C-IGP1 sites.

Elements	Warm				Cold			
	Mean	S.D	Min.	Max.	Mean	S.D	Min.	Max.
U-IGP1								

Al	0.913	5.748	BDL	100.059	0.262	0.505	BDL	4.541
Si	0.757	0.631	BDL	9.469	0.241	0.297	BDL	2.654
S	5.864	4.509	BDL	39.444	8.515	5.370	0.907	35.642
Cl	4.582	8.132	BDL	67.266	9.169	7.561	0.099	48.579
K	4.090	6.496	BDL	97.896	2.334	1.332	0.365	9.434
Ca	0.613	0.355	BDL	2.611	0.358	0.275	0.002	1.908
Ti	0.050	0.030	BDL	0.357	0.031	0.020	0.002	0.150
V	0.001	0.003	BDL	0.069	0.001	0.001	BDL	0.006
Cr	0.004	0.004	BDL	0.046	0.005	0.006	BDL	0.060
Mn	0.025	0.020	BDL	0.244	0.028	0.031	BDL	0.330
Fe	0.673	0.362	0.004	2.118	0.508	0.353	0.048	2.656
Ni	0.001	0.001	BDL	0.014	0.001	0.002	BDL	0.026
Cu	0.046	0.049	BDL	0.371	0.087	0.199	0.001	2.081
Zn	0.490	0.370	BDL	3.799	0.548	0.456	0.035	4.886
As	0.005	0.005	BDL	0.080	0.004	0.002	BDL	0.021
Se	0.004	0.006	BDL	0.084	0.003	0.003	BDL	0.042
Br	0.062	0.058	BDL	0.353	0.064	0.077	0.002	0.698
Rb	0.001	0.002	BDL	0.011	0.001	0.002	BDL	0.012
Sr	0.020	0.141	BDL	2.624	0.002	0.002	BDL	0.022
Zr	0.002	0.003	BDL	0.018	0.001	0.002	BDL	0.014
Cd	0.003	0.005	BDL	0.058	0.004	0.009	BDL	0.129
In	0.005	0.004	BDL	0.027	0.004	0.004	BDL	0.021
Sn	0.017	0.047	BDL	0.570	0.013	0.028	BDL	0.540
Sb	0.023	0.032	BDL	0.871	0.024	0.022	BDL	0.271
Ba	0.222	1.685	BDL	29.591	0.013	0.030	BDL	0.362
Pb	0.489	1.113	BDL	10.679	0.419	0.778	0.008	9.243
Bi	0.001	0.012	BDL	0.207	BDL	BDL	BDL	0.002
U-IGP2								
Al	1.089	4.075	BDL	87.500	0.629	0.511	BDL	3.093
Si	0.586	0.503	BDL	3.017	0.238	0.351	BDL	1.891
S	5.339	4.038	0.352	48.728	8.985	5.979	BDL	33.852
Cl	5.082	7.257	BDL	44.087	5.817	5.014	BDL	42.367
K	3.037	4.654	0.130	100.092	1.694	0.933	BDL	6.229
Ca	0.456	0.323	BDL	1.952	0.315	0.310	BDL	1.654
Ti	0.048	0.240	BDL	7.181	0.029	0.024	0.001	0.167
V	0.004	0.084	BDL	2.430	0.001	0.001	BDL	0.010
Cr	0.006	0.009	BDL	0.107	0.007	0.009	BDL	0.087
Mn	0.027	0.032	BDL	0.391	0.030	0.036	BDL	0.356
Fe	0.509	0.320	0.032	3.083	0.414	0.351	0.002	2.661
Co	BDL	0.000	BDL	0.002	BDL	BDL	BDL	0.002
Ni	0.002	0.003	BDL	0.044	0.002	0.002	BDL	0.022
Cu	0.075	0.204	0.001	3.490	0.088	0.149	BDL	1.741
Zn	0.588	0.514	0.012	4.316	0.609	0.474	0.001	3.151
As	0.009	0.009	BDL	0.083	0.011	0.007	BDL	0.068
Se	0.003	0.004	BDL	0.062	0.002	0.002	BDL	0.029
Br	0.070	0.086	0.001	1.100	0.055	0.050	BDL	0.578
Rb	0.001	0.002	BDL	0.010	0.001	0.002	BDL	0.013
Sr	0.018	0.144	BDL	3.905	0.002	0.002	BDL	0.017

Zr	0.001	0.001	BDL	0.012	0.001	0.001	BDL	0.007
Mo	0.0002	0.001	BDL	0.017	BDL	0.001	BDL	0.012
Cd	0.006	0.017	BDL	0.199	0.005	0.018	BDL	0.328
In	0.004	0.003	BDL	0.025	0.004	0.003	BDL	0.024
Sn	0.018	0.038	BDL	0.673	0.017	0.041	BDL	0.880
Sb	0.025	0.125	BDL	3.205	0.026	0.074	BDL	0.909
Te	0.014	0.011	BDL	0.081	0.014	0.010	BDL	0.053
Ba	0.190	1.401	BDL	29.346	0.008	0.014	BDL	0.122
Pb	0.441	1.032	0.010	14.654	0.386	0.577	BDL	6.978
Bi	0.001	0.014	BDL	0.455	BDL	BDL	BDL	0.009
C-IGP1								
Al	0.644	1.930	BDL	23.082	0.068	0.732	BDL	21.263
Si	3.733	5.039	BDL	52.857	0.175	0.277	BDL	2.880
S	2.269	1.282	0.003	7.683	4.933	2.510	BDL	17.815
Cl	1.347	2.360	0.003	27.881	5.423	5.742	BDL	40.687
K	1.971	1.469	0.005	13.694	2.069	1.321	0.005	14.165
Ca	1.150	1.452	0.002	16.163	0.203	0.197	BDL	2.032
Ti	0.098	0.115	BDL	1.305	0.018	0.014	BDL	0.143
V	0.002	0.004	BDL	0.039	BDL	0.000	BDL	0.004
Cr	0.002	0.004	BDL	0.049	0.001	0.002	BDL	0.047
Mn	0.021	0.026	BDL	0.298	0.008	0.006	BDL	0.070
Fe	1.028	1.204	0.007	13.561	0.223	0.147	0.003	1.525
Ni	0.001	0.002	BDL	0.016	BDL	0.001	BDL	0.024
Cu	0.018	0.038	BDL	0.484	0.025	0.046	BDL	0.918
Zn	0.158	0.163	BDL	2.402	0.201	0.137	BDL	0.858
As	0.002	0.003	BDL	0.047	0.002	0.002	BDL	0.016
Se	0.001	0.001	BDL	0.012	0.001	0.001	BDL	0.015
Br	0.025	0.020	BDL	0.419	0.037	0.295	BDL	8.855
Rb	0.004	0.005	BDL	0.050	0.002	0.003	BDL	0.026
Sr	0.008	0.010	BDL	0.102	0.001	0.003	BDL	0.070
Zr	0.001	0.003	BDL	0.037	BDL	BDL	BDL	0.006
Cd	0.002	0.005	BDL	0.144	0.002	0.003	BDL	0.027
Sn	0.006	0.005	BDL	0.034	0.006	0.015	BDL	0.414
Sb	0.017	0.030	BDL	0.978	0.018	0.020	BDL	0.361
Ba	0.002	0.009	BDL	0.241	0.004	0.034	BDL	0.789
Pb	0.053	0.074	BDL	1.365	0.076	0.049	BDL	0.328

Table S3: Mean concentration($\mu g.m^{-3}$) of the elemental sources and PMel during the day and night of the warm and cold periods at U-IGP1, U-IGP2 and C-IGP1 sites.

	Warm (mean in $\mu g.m^{-3}$)			Cold (mean in $\mu g.m^{-3}$)		
Sources	Day	Night	Overall	Day	Night	Overall
U-IGP1						
SFC1	3.84	3.95	3.89	1.71	2.23	1.97
SFC2	0.48	0.42	0.45	0.54	0.42	0.48

Cl-rich	3.93	4.99	4.46	8.29	11.37	9.83
S-rich	3.93	2.98	3.45	8.02	6.15	7.09
Cu-rich	0.32	0.43	0.37	0.70	0.97	0.83
Coal Comb.	0.89	1.56	1.23	0.85	1.14	1.00
Dust	1.72	2.03	1.88	1.15	1.25	1.20
PM_el	15.12	16.36	15.74	21.27	23.52	22.40
U-IGP2						
SFC1	3.04	3.63	3.33	1.65	2.10	1.87
SFC2	0.57	0.65	0.61	0.66	0.73	0.69
Cl-rich	3.76	6.44	5.10	5.02	7.10	6.06
S-rich	3.38	2.87	3.13	7.92	7.62	7.77
Cu-rich	0.18	0.46	0.32	0.26	0.52	0.39
Coal Comb.	0.63	1.07	0.85	0.60	0.82	0.71
Dust	1.41	1.76	1.59	1.06	1.29	1.18
PM_el	12.97	16.88	14.92	17.17	20.18	18.68
C-IGP1						
SFC1	1.30	1.98	1.64	0.95	1.19	1.07
SFC2	0.37	0.34	0.35	0.46	0.42	0.44
Cl-rich	0.79	1.59	1.19	4.45	7.28	5.86
S-rich	2.11	1.72	1.92	4.66	5.04	4.85
Cu-rich	0.04	0.10	0.07	0.07	0.12	0.09
Coal Comb.	0.19	0.23	0.21	0.17	0.17	0.17
Dust	5.77	5.86	5.81	0.61	0.44	0.53
PM_el	10.58	11.81	11.19	11.36	14.65	13.01

Table S4: Mean concentration($\mu g.m^{-3}$) of the PM2.5, PMel and the meteorological parameters during various episodes at U-IGP1, U-IGP2 and C-IGP1 sites.

	Warm			Cold		
	C1	EP1	EP2	C2	EP3	EP4
U-IGP1						
$PM_{2.5}$ ($\mu g.m^{-3}$)	43.3	289.5	242.9	42.2	185.3	251.6
PM_{EI} ($\mu g.m^{-3}$)	5.7	31.4	31.8	6.1	19.8	34.3
$PM_{EI}/PM_{2.5}$	0.1	0.1	0.1	0.2	0.1	0.1
WS (m/s)	4.4	4.1	5.2	5.0	3.1	3.3
WD	226.2	251.4	290.9	124.7	181.6	171.1
SR (W/m^2)	111.9	63.8	78.4	63.7	67.7	59.0
PBLH (m)	500.8	464.3	476.7	349.9	356.4	320.7
RH (%)	79.7	73.0	67.0	83.2	77.3	82.3
Temp. (°C)	26.2	23.3	21.5	19.1	15.3	8.7
U-IGP2						
$PM_{2.5}$ ($\mu g.m^{-3}$)	41.3	370.5	302.0	46.6	250.6	265.2
PM_{EI} ($\mu g.m^{-3}$)	5.2	27.6	32.5	5.3	22.9	27.7

PM$_{EI}$/PM$_{2.5}$	0.1	0.1	0.1	0.1	0.1	0.1
WS (m/s)	1.1	0.8	0.9	1.0	0.7	1.0
WD	253.9	252.3	263.7	226.9	249.3	234.1
SR (W/m^2)	169.9	75.0	95.0	72.8	68.7	61.4
PBLH (m)	570.6	487.4	496.1	355.8	333.2	386.3
RH (%)	72.7	77.5	67.9	86.8	68.6	85.1
Temp. (°C)	25.8	19.9	22.6	10.5	24.1	9.9
C-IGP1						
PM$_{2.5}$ (µg.m^{-3})	31.2	89.1	91.5	51.9	243.4	202.1
PM$_{EI}$ (µg.m^{-3})	5.3	20.6	25.1	6.1	21.5	16.5
PM$_{EI}$/PM$_{2.5}$	0.2	0.2	0.3	0.1	0.1	0.1
WS (m/s)	1.3	1.0	2.6	1.1	0.4	0.8
WD	166.4	133.2	196.3	136.9	146.9	174.1
SR (W/m^2)	232.4	173.3	184.6	111.6	101.3	80.1
PBLH (m)	839.7	656.3	529.0	353.6	364.7	167.9
RH (%)	44.1	49.7	45.9	76.0	73.3	77.4
Temp. (°C)	27.1	25.2	27.6	19.4	13.8	15.5

Table S5: Correlation among the similar resolved factor profile at all the three sites.

Source Profiles	b/w U-IGP1 and U-IGP2	b/w U-IGP1 and C-IGP1	b/w U-IGP2 and C-IGP1
Cl-rich	1	1	1
Coal Comb.	0.98	0.6	0.6
Cu_rich	0.92	0.5	0.6
Dust related	0.99	0.87	0.9
SFC1	0.98	0.99	0.96
SFC2	0.99	0.6	0.7
S-rich	1	1	0.99

Table S6: Duration of clean and pollution episodes at the three IGP sites

Period	Episodes	U-IGP1	U-IGP2	C-IGP1
Warm	C1	1st Oct-08th Oct	1st Oct-08th Oct	22nd Apr-26th Apr
	EP1	31st Oct-04th Nov	30th Oct-04th Nov	17th Mar-22nd Mar
	EP2	09th Nov-17th Nov	09th Nov-16th Nov	06th Apr-08th Apr
	C2	27th Nov-29th Nov	27th Nov-29th Nov	07th Jan

Cold	EP3	03rd Dec-13th Dec	05th Dec-12th Dec	19th Dec-24th Dec
	EP4	26th Dec-03rd Jan	25th Dec-31st Dec	01st Jan-05th Jan

References

Canonaco, F., Tobler, A., Chen, G., Sosedova, Y., Slowik, J. G., Bozzetti, C., Daellenbach, K. R., ElHaddad, I., Crippa, M., Huang, R.-J., Furger, M., Baltensperger, U., & Prévôt, A. S. H. (2020). A new method for long-term source apportionment with time-dependent factor profiles and uncertainty assessment using SoFi Pro: application to one year of organic aerosol data. *Atmospheric Measurement Techniques Discussions*, 1–39. https://doi.org/10.5194/amt-2020-204

Cui, W., Meng, Q., Feng, Q., Zhou, L., Cui, Y., & Li, W. (2019). Occurrence and release of cadmium, chromium, and lead from stone coal combustion. *International Journal of Coal Science and Technology*, *6*(4), 586–594. https://doi.org/10.1007/S40789-019-00281-4/FIGURES/4

Jin, R., Zheng, M., Lammel, G., Bandowe, B. A. M., & Liu, G. (2020). Chlorinated and brominated polycyclic aromatic hydrocarbons: Sources, formation mechanisms, and occurrence in the environment. *Progress in Energy and Combustion Science*, *76*, 100803. https://doi.org/10.1016/J.PECS.2019.100803

Manchanda, C., Kumar, M., Singh, V., Hazarika, N., Faisal, M., Lalchandani, V., Shukla, A., Dave, J., Rastogi, N., & Tripathi, S. N. (2022). Chemical speciation and source apportionment of ambient PM2.5 in New Delhi before, during, and after the Diwali fireworks. *Atmospheric Pollution Research*, *13*(6), 101428. https://doi.org/10.1016/J.APR.2022.101428

Rai, P., Furger, M., El Haddad, I., Kumar, V., Wang, L., Singh, A., Dixit, K., Bhattu, D., Petit, J. E., Ganguly, D., Rastogi, N., Baltensperger, U., Tripathi, S. N., Slowik, J. G., & Prévôt, A. S. H. (2020). Real-time measurement and source apportionment of elements in Delhi's atmosphere. *Science of The Total Environment*, *742*, 140332. https://doi.org/10.1016/J.SCITOTENV.2020.140332

Stefenelli, G., Pospisilova, V., Lopez-Hilfiker, F. D., Daellenbach, K. R., Hüglin, C., Tong, Y., Baltensperger, U., Prévôt, A. S. H., & Slowik, J. G. (2019). Organic aerosol source apportionment

in Zurich using an extractive electrospray ionization time-of-flight mass spectrometer (EESI-TOF-MS) – Part 1: Biogenic influences and day–night chemistry in summer. *Atmospheric Chemistry and Physics*, *19*(23), 14825–14848. https://doi.org/10.5194/acp-19-14825-2019